THESIS

IMPROVED CHARACTERIZATION OF NATURAL GAS LEAK PLUMES USING A LAPLACE TRANSFORM APPROACH TO CORRECT FOR INSTRUMENT RESPONSE TIME

Submitted by

Thomas E. O'Brien

Department of Mechanical Engineering

In partial fulfillment of the requirements

For the Degree of Master of Science

Colorado State University

Fort Collins, Colorado

Fall 2021

Master's Committee:

Advisor: Anthony Marchese
Co-Advisor: Joe von Fischer

Mohammad Abutayeh
Zachary Weller

ABSTRACT

IMPROVED CHARACTERIZATION OF NATURAL GAS LEAK PLUMES USING A LAPLACE TRANSFORM APPROACH TO CORRECT FOR INSTRUMENT RESPONSE TIME

The response time of an instrument is a measure of how quickly it achieves a steady-state value in response to a step change input. The response time directly affects the accuracy of reported values when the instrument is subject to transient conditions. In methane leak surveying, methane gas concentrations are often measured from instruments mounted in moving vehicles. The methane concentrations detected by those instruments are therefore constantly varying. Depending on the physical size of the methane plume, vehicle speed and instrument response time, a vehicle-mounted instrument may or may not reach a steady-state value as the instrument inlet traverses the plume, which can result in an underestimation of the true ambient gas concentration of the plume. For leak detection techniques that rely on downwind concentration measurements to estimate an emission rate and/or detect the presence of a methane emission source, this issue can result in underestimation of emission rates and/or failure to detect an emission source. Further complicating these efforts, different gas analyzers often have different time response characteristics, resulting in an ambiguity in readings achieved by different instruments. In this research, a model was developed to generate improved estimates of the actual gas concentration values and waveform shapes using Laplace transforms, given the time response characteristics of the instruments. Several methane gas analysis instruments used for methane leak detection surveying were experimentally characterized in a laboratory setting to determine their time response characteristics. Controlled release field testing in conjunction with simultaneous methane measurements from multiple instruments mounted on the same moving vehicle were then used to validate this methodology. During field testing, instruments with different response

characteristics were plumbed in parallel, thereby sampling the same air stream. The results indicated that the instrument with a faster response time consistently reported significantly higher peak methane concentrations than the slower response instrument. However, by applying the model developed in this study to the raw time-varying gas concentration data, the corrected concentration profiles for the two instruments were found to be nearly identical. The results also indicate that the raw signals from both instruments underrepresented the actual peak methane concentrations for the majority of detected plumes. The results of this study suggest the importance of accurately accounting for instrument time response in downwind, vehicle-mounted methane measurement techniques to ensure that peak methane concentrations are not underreported.

TABLE OF CONTENTS

LIST OF TABLES

LIST OF FIGURES

INTRODUCTION

As the world continues to seek innovative ways to reduce to the production of carbon dioxide through means such as renewable energy and electric vehicles, other sources of greenhouse gasses are sometimes overlooked. One such source is the infrastructure surrounding natural gas (NG). This infrastructure includes production and distribution systems such as the wells and pipelines, all the way down to systems located at the consumer end, such as meters or appliances. Methane, the main component of natural gas, is an extremely potent greenhouse gas compared to carbon dioxide, especially considered over a short time span [1-3]. Quantifying the amount of gas lost from the NG infrastructure is notoriously difficult, as NG leaks are not the only source of atmospheric methane. Methane emissions can be sourced to two main groups, fossil and biogenic. Fossil methane, the kind found in natural gas, is the mined or welled byproduct of organisms trapped underground for millions of years. Biogenic methane is produced naturally and continuously from current ecosystems, such as swamps and marshes, or from agricultural sources, such as livestock.

A simple method for distinguishing between biogenic and fossil sources involves consideration of the additional components of natural gas. Methane is the primary gas composing natural gas, but natural gas also contains ethane, propane, butane, and pentane. By considering these additional components in a survey of the natural gas system, methane sources can be determined to be biogenic or fossil [4]. A more complex approach based on nuclear science can be considered as well. Though both fossil and biogenic sources produce methane, they differ in one important way – biogenic methane contains Carbon-14, which is constantly replenished in the atmosphere by cosmic rays. This radioactive isotope has a relatively short half-life which means that fossil methane, which has been sequestered underground for time periods much longer than this half-life, does not contain this isotope. This important characterization allows a methane source to be definitively identified as fossil or biogenic in

nature. Unfortunately, Carbon-14 is also produced in trace amounts by certain types of nuclear power plants [5], which complicates this analysis method. To overcome these difficulties, a research group conducted analysis on pockets of air found in ice core samples dated to be from the pre-industrial era [6]. By conducting gas measurements on these air pockets, an estimate was made on the amount of biogenic methane produced. These measurements showed that other estimations of biogenic methane, which are based on air samples from the modern era, are, in fact, overestimations. Therefore, the amount of fossil methane being released into the atmosphere is often underestimated. Corroborating this research, another team estimated the amount of fossil methane released by using ground-based and aerial survey techniques [7]. This research quantified the natural gas lost to be equal to 2.3% of the total natural gas production in the United States, which is approximately equal to an astonishing 13 teragrams per year.

As a result of the inherent complexity of the natural gas infrastructure it is not necessarily easy to eliminate the problem of gas leakage. In fact, the exact condition of infrastructure subsections can have a large effect on their propensity to leak. For instance, cities like Boston and Washington, DC, which have older NG pipelines constructed with more corrosion-prone materials such as cast iron, have higher leak rates [8, 9]. These distribution systems not only consist of a complicated network of underground pipelines, but also of a variety of components. Additionally, methane sources can interfere with one another. These considerations result in a complicated and extensive process to locate and eliminate leaks from the NG infrastructure in the United States. To that end, research has been conducted using instrumented vehicles to detect and locate natural gas leaks in urban NG distribution systems [10, 11]. These vehicles are equipped with a variety of sensors, such as high-resolution GPS, 2D anemometer, and highly sensitive gas analyzers capable of measuring methane concentration, typically at ppb-level precision and accuracy. This combination of instrumentation generates a rich data set that allows the mapping of methane concentrations throughout a city, when combined with meteorological

data. Analysis of these data allows natural gas leaks to be discovered, characterized in terms of emission rate, and ultimately located [10-12]. Extensive processing is required to analyze the vast amount of data produced during each mapping operation. Consequently, it is important to ensure that the instruments are properly configured and deployed to produce data that are most representative of the true conditions at the measurement location.

One of the most critical components of the mapping process is the gas analyzer. To produce the most accurate results, this instrument should have the capability to measure the concentration of methane quickly and accurately, ideally to the PPB level, under a diverse set of conditions. Typically, the ambient concentration of methane is around 2 PPM. When the vehicle drives through a natural gas plume created by a leak, the sensor will measure a rise in local methane concentration. Occasionally, this concentration will only rise by a small amount – perhaps by only one or two PPM. However, depending on the size of the leak, the vehicle's relative position, as well as the meteorological conditions, these spikes can rise to values as high as several hundred PPM [11]. Likewise, the detection period of the leak, or the length of time the concentration of methane rises above a certain threshold with respect to the ambient background concentration can vary substantially as well.

Two main gas analyzer systems have been developed and deployed for methane mapping – closed-path and open-path. High-precision instruments such as the Aeris and the LGR use laser absorption spectroscopy which is the latest best standard for high-precision and accuracy for CH4 detection. However, these instruments use internal lasers, detectors, and pumped sampling so they do not have fast response in comparison to open-path instruments such as the LiCor 7700. As the name implies, open-path sensors have a measurement path open to the atmosphere that the laser passes through. This device involves no pumping mechanism and relies solely on air passing through the path of the laser. On the other hand, closed-path sensors require plumbing and pumps to move sample air through the analytical cell where the CH4 concentration is determined. Depending on the length and

size of the plumbing involved, the flow rate of the pump, and the volume of the sampling cell, significant time lag and dampening effects can occur in the resulting data signal compared to an ideal direct measurement. While a fast pump can be used to minimize these effects, it should be combined with a sensing module that can accurately measure the gas components of the resulting gas flow.

Open-path sensors do not involve pumps or plumbing. Consequently, the instrument lag and response times of these sensors are quite small. However, since open-path sensors are fully exposed to the atmosphere, the sensor path can become obstructed by particulate matter or water. These effects prevent the instrument from being used in adverse weather conditions, such as rain. Additionally, these open-path sensors can be quite large. Because the data acquired in this research is taken from a moving vehicle, the cumbersome and sensitive nature of the open-path instruments is not ideal. Therefore, closed-path sensors have been used for the data collection described in this research. These sensors allow small inlets to be mounted on the front bumper of the vehicle, with the actual sensing unit located in the trunk. While this configuration does allow data to be collected from a vehicle in a variety of conditions, it is still possible for the plumbing or filters of closed-path sensors to become clogged or obstructed, though this issue has not yet posed a problem in data collection.

As discussed, since closed-path instruments require the use of a pump, there is the possibility that the output data signal generated by the instrument may result in a dampened or reduced reading of the reported gas concentration. Ideally, this effect can be prevented by using a high-speed pump, combined with a fast-response instrument. Additionally, fast-response instruments are not necessarily high precision. Furthermore, many manufacturers do not advertise the specific response nature of the sensors used in their instruments. Another factor that can obfuscate the true ambient gas concentrations of the sampled air is the data sampling rate of the instrument. Because these instrument characteristics affect the reported methane concentrations, disagreements can arise between different types of gas analyzers, even when the instruments are sampling the same air and are properly

calibrated. This disagreement is most noticeable when comparing fast and slow-response instruments, even when both instruments have high precision. As gas analysis technology progresses, it will be beneficial to have the option to switch between different instruments. The analysis developed in this research provides a correction procedure to help reduce the differences between instruments with different response characteristics and sampling methods.

In order to accurately quantify methane leak rates and to successfully locate leak sources, methane measurements must be as accurate as possible. As discussed, methane detection signals can often be quite short-lived. Therefore, it is ideal to perform these measurements with a fast-response instrument using a high sampling rate. However, most methane measurement instruments do not provide high sampling rates. In fact, many closed-path instruments take measurements at a sampling rate of just 1 Hz, and all instruments used in this research record data at this frequency. These factors form the basis of the motivation to both characterize the response of a variety of instruments and perform a mathematical correction to the generated data to compensate for the slow response times.

The objectives of this research are to investigate whether measurements obtained with methane sampling instruments having different response characteristics can be corrected to achieve better agreement with known methane signals while also achieving better agreement between the various instruments. Improvements in measurement accuracy, especially methane peak concentrations will also greatly improve estimation of leak rates. In total, four instruments have been characterized. Two of these instruments are produced by Aeris Technologies, the Pico and the Ultra. The third instrument is produced by Los Gatos Research (LGR), and the final instrument is a Heath DP-IR+. Response times for the instruments are calculated from an experimental procedure that generates step inputs of a variety of gas concentrations to each instrument. The generated data is analyzed with computer software to calculate the time response characteristics of the instrument. Finally, using Laplace Transforms, an analytical regime is developed to estimate the true ambient gas concentration

signal that the instrument was exposed to. This process helps to eliminate measurement dampening effects due to the time response characteristics of an instrument while also addressing the issue of measurement ambiguity between different models of closed-path gas analysis instruments and between multiple survey vehicles.

CHAPTER 1. THEORY

Principal Mathematics

The methods discussed in this section are designed to provide an estimate of the true time-dependent variation in ambient gas concentration based on measurements obtained with gas sampling instruments that have specific time response characteristics, depending on the instrument.

The instruments discussed in this paper all follow an exponential time response curve. The simplest case for the instrument response to a step input can be modelled as a function of time as follows [13]:

$$C_i(t) = C_F + (C_I - C_F) \cdot e^{-\frac{t}{\tau}} \quad (1)$$

Where $C_i(t)$ represents the instrument's concentration reading in time and C_F and C_I represent the final and initial concentrations, respectively and τ represents the first-order time constant. Here, the value of τ is the time value at the point where 63.2% of the measured change in concentration is achieved in response to a step input. However, this function is not very useful for input-output analysis where the system inputs can be an arbitrary function of time. Instead, it is useful to determine a methodology that can predict the output for any arbitrary input. This can be done in two ways: by using Laplace transforms to create a transfer function or by using a numerical scheme. Both methods require the impulse response function of the system, as the numerical scheme involves the convolution of the impulse response, and the system input function and transfer functions involve the Laplace transform of this convolution.

As discussed by McCarthy [13], if equation 1 is considered to be the step response of the input, the impulse response function can be determined from the step response, which is defined as the integral of the impulse response function *δ(t)*. If equation 1 is scaled to be a unit step response, it can be equated to the impulse response function as follows.

$$1 - e^{-\frac{t}{\tau}} = \int_0^t \delta(t-\lambda)d\lambda \quad (2a)$$

To simplify the right-hand side of Eqn. (2a), define a new variable $z = \lambda - t$, from which $dz = d\lambda$ (λ is the variable of integration) and applying the symmetry property of the Dirac/delta function: $\delta(-z) = \delta(z)$ yields

$$1 - e^{-\frac{t}{\tau}} = \int_0^t \delta(t-\lambda)d\lambda = \int_0^t \delta(-\mathrm{z})dz = \int_0^t \delta(\mathrm{z})dz \quad (2b)$$

By differentiating both sides of this equation and invoking the fundamental theorem of calculus, the impulse response function can therefore be determined as

$$\delta(t) = \frac{e^{-\frac{t}{\tau}}}{\tau} \quad (3)$$

This response can be convoluted with an arbitrary input function. In this case, the input function is the unknown time-dependent ambient gas concentration, denoted as $C_a(t)$, which can be determined based on the measured instrument response. The convolution (designated by the operator $*$) is equal to the instrument response, $C_i(t)$.

$$C_i(t) = C_a(t) * \delta(t) = \int_0^t C_a(\lambda) \cdot \delta(t-\lambda)d\lambda \quad (4)$$

At this point, two different approaches can be used to solve for the ambient concentration. Equation 4 could be differentiated, and $C_a(t)$ could be determined numerically. This approach was used by McCarthy [13], as well Arieli and Van Liew [14], whose method has been used in various works [15, 16]. However, this method consists of a numerical scheme involving finite differences, and the mathematical equations can become difficult to solve when more complex models with multiple time constants are developed, which will be discussed later. The present work instead uses Laplace transforms to determine a transfer function for the instrumentation, similar in concept to the method discussed by Sirs [17]. For the simple case illustrated in equation 4, the transfer function, $H(t)$, for the instrument can be determined by taking the Laplace transform of the convolution integral and dividing both sides by the Laplace transform of the $C_a(t)$ term.

$$H(s) = \frac{\mathcal{L}\{C_i(t)\}}{\mathcal{L}\{C_a(t)\}} = \mathcal{L}\{\delta(t)\} \quad (5)$$

$$H(s) = \frac{C_i(s)}{C_a(s)} = \frac{1}{\tau} \cdot \frac{1}{s+\frac{1}{\tau}} = \frac{1}{\tau s+1} \quad (6)$$

Equation 6 can then be used in a computer simulation to determine the instrument response to any input. This procedure can be useful for a variety of reasons. By subjecting an instrument to a specific test and comparing the results to the simulated response to the same input generated by the model, the accuracy of the model parameters can be determined and adjusted as needed. This method is used to generate the models for the instruments tested in this paper, to be discussed later. Additionally, these simulations can describe how a system responds to a variety of inputs, providing insight into the dynamic capabilities of the instrument.

This concept is the basis of determining the true time-resolved ambient gas concentration, C_a, from the raw time series data generated by the instrument. Once the model is properly tuned to best replicate the performance of the instrument, C_a can be determined by the reciprocal of the transform.

$$H_{\mathrm{a}}(s) = \frac{C_{\mathrm{a}}(s)}{C_{\mathrm{i}}(s)} = \frac{\tau s+1}{1} \quad (7)$$

However, due to the nature of Laplace transforms in the continuous domain, simply taking the reciprocal of the transform results in a non-causal model. In the Laplace space, poles are the roots of the open-loop transfer function in the denominator, while zeros are the roots of the open-loop transfer function in the numerator. In a transfer function, there cannot be more zeros than poles, which is what results if the reciprocal transfer function is used. Therefore, to estimate the input values from the reciprocal transfer function, there must be an approximation function added to the denominator, again resulting in more poles than zeros. This situation is similar in concept to the approximations that are obtained using numerical schemes, such as the finite-difference method. This approximation function should be small, much smaller than the time response of the instrument. These fast dynamics are added in the form of a second order polynomial, similar in form to a mass-spring-damper system.

Note, for simplicity, the factor of two that is traditionally included in mass-spring-damper systems on the $\zeta \cdot \beta$ term is not used here.

$$H_{\mathrm{a}}(s) = \frac{C_{\mathrm{a}}(s)}{C_{\mathrm{i}}(s)} = \frac{\tau s+1}{1} \cdot \left(\frac{1}{(\beta \mathrm{s})^2+(\zeta \cdot \beta) \cdot \mathrm{s}+1}\right)^{\mathrm{n}} \quad (8)$$

Here, β is the described approximation factor, ζ is a damping factor used to remove noise, and n is an exponent used to adjust the total number of poles in the system. For the simple, single-time-constant case demonstrated in equation 8, the n value would only need to be set to one, as this would yield a greater number of poles than zeros.

While single-time-constant models work well, many instruments can be better modelled with multiple time constants. The use of multiple time constants improves the accuracy of the instrument output models and consequently the estimation of the true methane signal. Multiple time constants account for instrument-specific characteristics such as the effects of the sampling reservoir, sensor dynamics and pump characteristics. Multiple time constants are better able to model certain aspects of the instrument response that may be present, such as overshoots or oscillations. In this paper, all instruments are modelled with 3 time constants, as follows.

$$H(s) = \frac{1}{(\tau_1 s+1) \cdot (\tau_2 s+1) \cdot (\tau_3 s+1)} \quad (9)$$

In this case, the input estimation requires an n value of at least two to ensure that the total number of poles is greater than the total number of zeroes.

$$H_{\mathrm{a}}(s) = \frac{C_{\mathrm{a}}(s)}{C_{\mathrm{i}}(s)} = \frac{(\tau_1 s+1) \cdot (\tau_2 s+1) \cdot (\tau_3 s+1)}{1} \cdot \left(\frac{1}{(\beta \mathrm{s})^2+(\zeta \cdot \beta) \cdot \mathrm{s}+1}\right)^{\mathrm{n}} \quad (10)$$

By providing equations 9 and 10 to a dynamic system response simulator, the simulated response of an instrument to an arbitrary input, as well as the input estimation for real experimental data, can be obtained.

Analytical Verification of Mathematics

The mathematical processes used to estimate the input of a system can be verified in an analytical simulation. This can be done by analytically simulating the output response of a system based on specified time-response characteristics and then using that output to estimate the known original input. In this paper, this analysis has been done within MATLAB (2021a) using the `lsim` command. A standard test protocol was developed, shown in Figure 1, both for this analytical verification, and for the experimental instrument characterization (to be discussed in a future section).

The test consists of introducing specific gas concentrations to flow through the system for various times, ranging from 60 seconds to just a few seconds. The various flow times are highly useful for accurately modelling the analyzer's time response. The longer flow times aid in determining the time it takes for the system to reach a steady-state reading, while the shorter bursts of gas help characterize

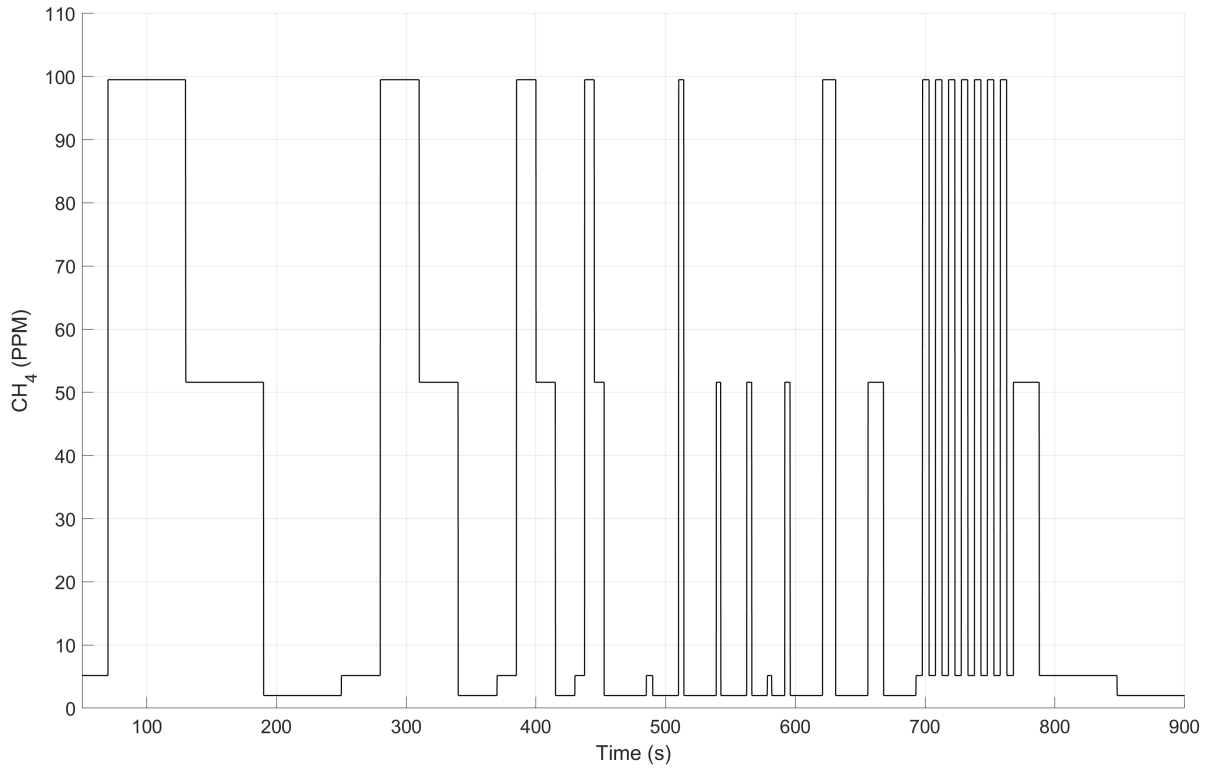

Figure 1. Standard instrument characterization test protocol used for both analytical verification and experimental instrument characterization. Includes multiple CH4 concentration levels and duration.

how the analyzer behaves when a steady state value is not achieved, which is often the case for field measurements. Three methane gas concentrations were used for the characterizations: (2, 5, and 100 PPM) corresponding to the range of gas concentrations typically seen by analyzers doing natural gas leak surveys.

Consider the following two systems, one with slow response characteristics, and one with considerably faster dynamics. The systems have the following time constants, measured in seconds.

$$\text{System 1: } \tau_1 = 0.7 \text{ s}, \tau_2 = 0.65 \text{ s}, \text{ and } \tau_3 = 3.8 \text{ s}$$

$$\text{System 2: } \tau_1 = 0.35 \text{ s}, \tau_2 = 0.38 \text{ s}, \text{ and } \tau_3 = 1.3 \text{ s}$$

The respective transfer functions for these systems are as follows.

$$H_1(s) = \frac{1}{(0.7s+1)\cdot(0.65s+1)\cdot(3.8s+1)} \tag{11a}$$

$$H_2(s) = \frac{1}{(0.35s+1)\cdot(0.38s+1)\cdot(1.3s+1)} \tag{11b}$$

By applying these transfer functions and the input shown in Figure 1 to `lsim` in MATLAB and simulating the response using a 10kHZ sampling rate, the plot shown in Figure 2 can be produced, showing the predicted response of these instruments to the test input.

The differences in the response characteristics of the two models can clearly be seen in Figure 2. As expected, the fast-response model, system 2, has quicker response times, resulting in the ability to nearly reach the steady-state input concentration even for the shortest duration inputs. For example, the fast system 2 response is most noticeable on one of the shortest duration inputs, occurring at around 540s. Here, system 2 reaches a maximum value of 45.74 PPM, 88.6% of the input concentration, while system 1 reaches 27.12 PPM, only 52.6% of the input. Both these systems are realistic representations of gas analysis instruments available on the market. The differences between the two models are illustrative of the real-world data acquisition problems that can occur with the natural gas survey techniques. If two different vehicle systems are acquiring data using different models of gas analyzers, even if all other vehicle systems are identical, comparing the data between the vehicles can

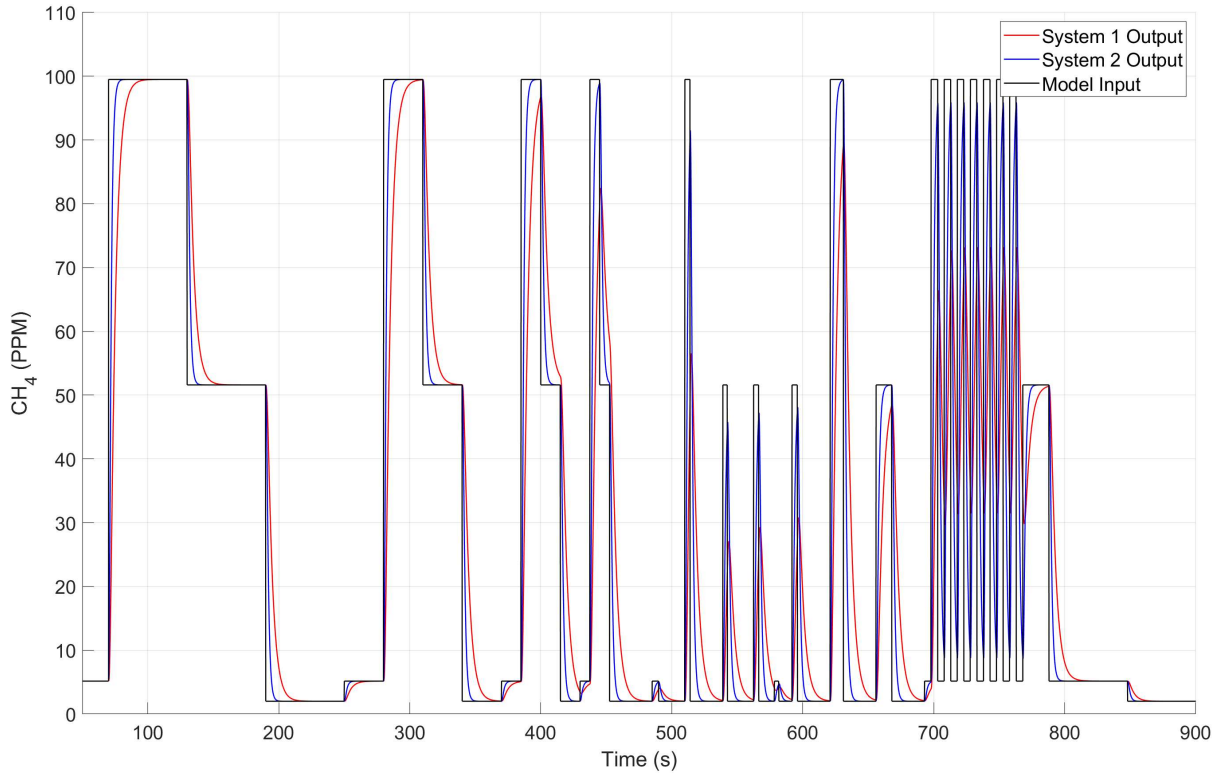

Figure 2. Simulated response of two arbitrary systems to the test protocol, showing the effects of instrument time response; system 1 has slower response than system 2.

pose a considerable challenge. For this reason, it is desirable to attempt to remove the time-response discrepancies from the instruments.

To estimate the input of these systems based on sampled data, the reciprocals of equations 11a and 11b are taken and the approximation function is applied, with $\beta = 0.01$ and $\zeta = 2$. This β factor value is much smaller than any of the time constants in the models and is used for all subsequent analysis. The ζ value is initially chosen to critically dampen the approximation function.

$$H_{1a}(s) = \frac{(0.7s+1)\cdot(0.65s+1)\cdot(3.8s+1)}{1} \cdot \left(\frac{1}{(0.01s)^2+(2\cdot 0.01)\cdot s+1}\right)^3 \quad (12a)$$

$$H_{2a}(s) = \frac{(0.35s+1)\cdot(0.38s+1)\cdot(1.3s+1)}{1} \cdot \left(\frac{1}{(0.01s)^2+(2\cdot 0.01)\cdot s+1}\right)^3 \quad (12b)$$

With these reciprocal transfer functions, the original input can be estimated, as shown in Figure 3. Both system input approximations, as well as the true input, are plotted here. Note that since the

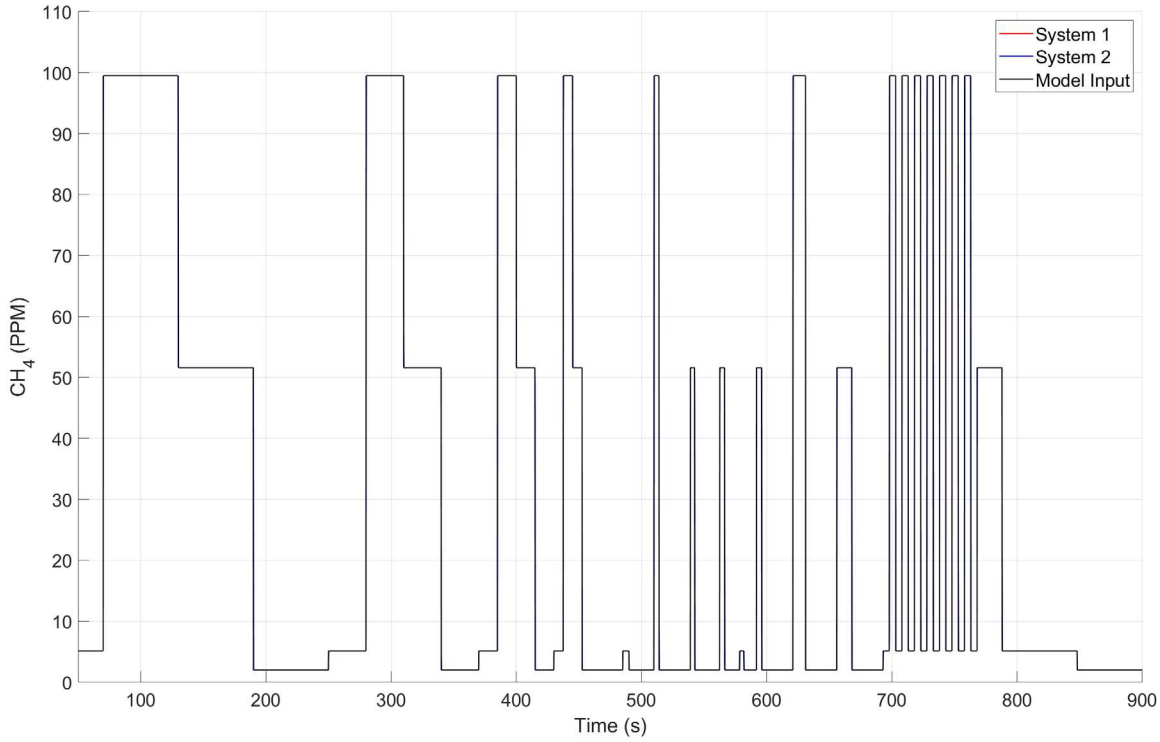

Figure 3. Input estimation of the simulated responses for high data sampling rate, demonstrating near perfect reproduction of the test protocol. Estimation curves for both systems lie directly on the test protocol.

input estimations work very well for high sampling rates with purely simulated data, the plots representing the estimated inputs appear to lie directly on top of the plot of the true input. However, the simulated sampling rate of 10kHz is not realistic in terms of real-world instrumentation. For instance, the instruments analyzed in this paper all record data at 1Hz, a significantly slower sampling rate than used in the simulation. This sampling rate can be easily replicated by downsampling the instrument output of the simulation to 1Hz resulting in a data stream similar to the data produced by the real-world instruments. In the analysis of the real instrument data (described in a later section), the recorded instrument data stream is interpolated to 100Hz using a piecewise cubic function. For analysis of the simulated instrument response, the downsampled data is also interpolated to 100Hz to replicate this process. The resulting system responses and the estimated inputs are presented in Figure 4. This figure clearly shows a significant amount of noise artifact. The 1 Hz downsampled data loses a significant

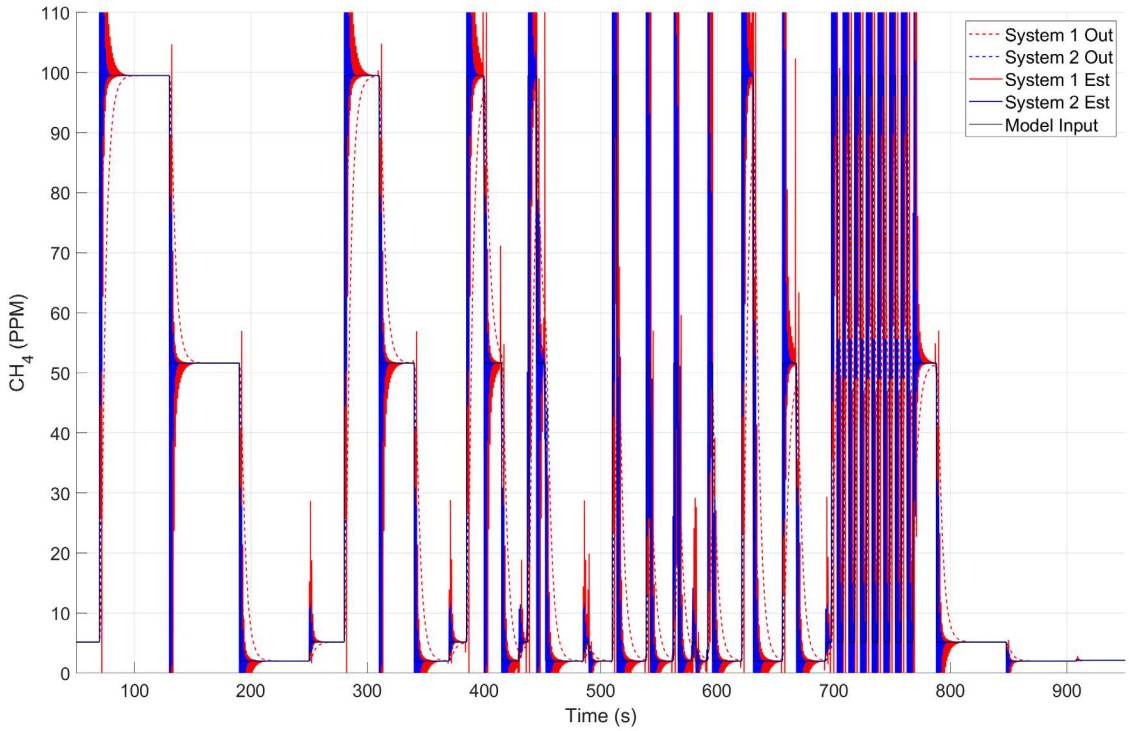

Figure 4. Simulated responses and corresponding input estimations using 1 Hz downsampled data, illustrating noise artifact produced by a low ζ value.

amount of fidelity, resulting in the generation of noise artifacts for the input analysis. Fortunately, this noise can be removed with an increase of the aforementioned ζ value. This value is increased for each system until the spikes, particularly noticeable in the cyclic square wave section near 700 s, do not exceed the maximum values of the true input. For systems 1 and 2, optimum ζ values were determined to be 64 and 50, respectively (ζ optimization method described in a later section). This process results in the plot shown in Figure 5

Clearly, the input estimations shown in Figure 5, obtained with the lower sampling rates, do not reproduce the true input waveform as closely as those obtained using the high-frequency data rate (Figure 3), but the estimated input is still much closer to the true input than the model output response. This improvement is most noticeable in the square wave section of the test, shown in detail in Figure 6. Once again, it is important to note the differences in response between the slow and fast models. The fast model nearly reaches the true input values, while the slow model begins to produce a sort of

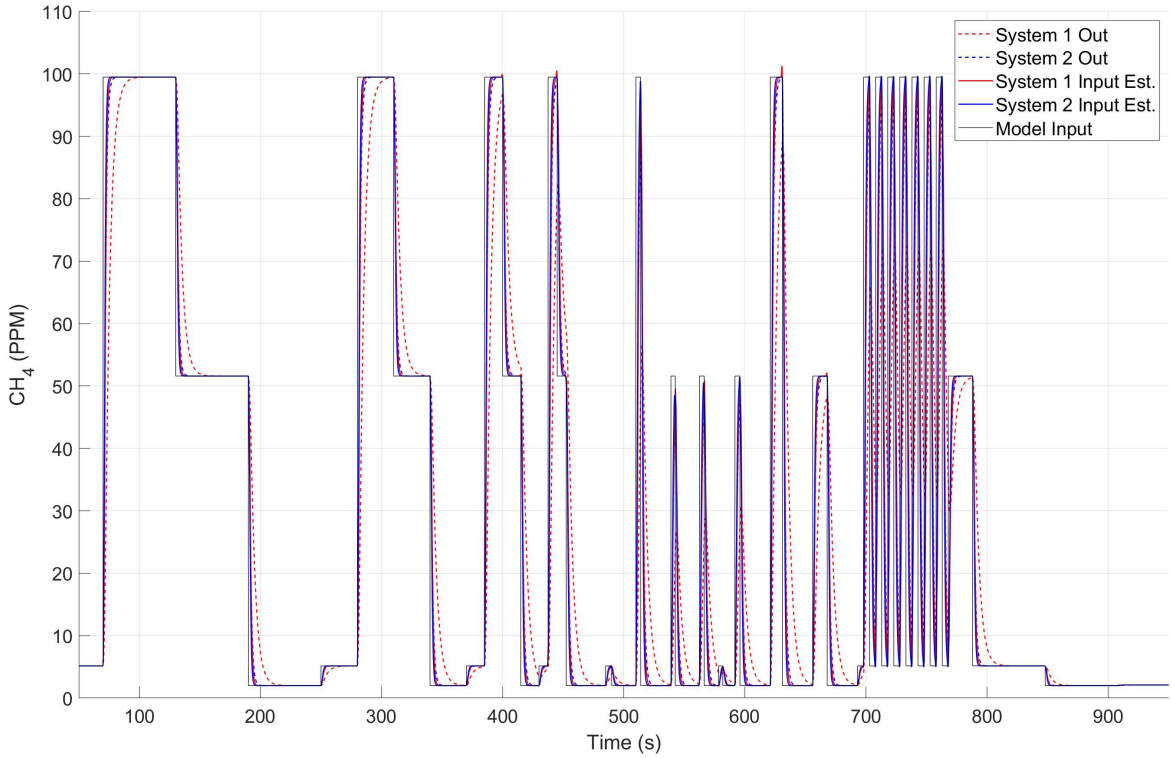

Figure 5. Simulated responses and corresponding input estimation using 1 Hz downsampled data with an optimized ζ value.

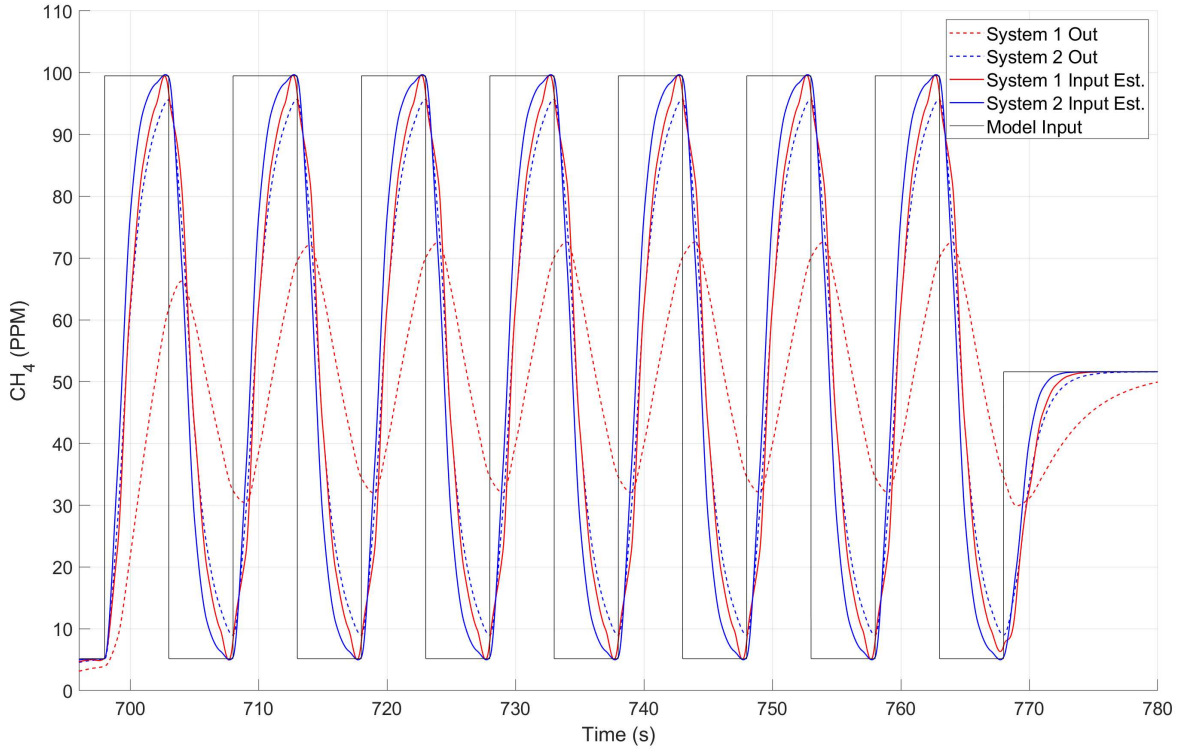

Figure 6. Detail of simulated responses and input estimation using 1 Hz downsampled data, with an optimized ζ value, centered on the square-wave section.

sinusoidal response centered near the average value of the square-wave. The input estimation analysis brings both systems to output the true maximum and minimum input values. While the estimated input reaches these maximum and minimum values, it does not produce the exact step-input, which was reproduced in Figure 3. Again, this is due to the lower resolution of the downsampled data, combined with the effects of the time response of the system, resulting in an inaccurate reproduction of the input wave form.

However, for many aspects of the leak detection data analysis, better estimation of the maximum gas concentration values is more important than the exact reproduction of the input signal waveform. As a final addition to the analytical verification, instrument noise is added to the signal. This is done by adding a random value between -0.1 and +0.1 PPM is added to every data point in the downsampled, 1Hz data stream, prior to interpolation. The results of noise addition can be seen in Figure 7. The noise doesn't cause a significant change in the estimated output, but it should be noted

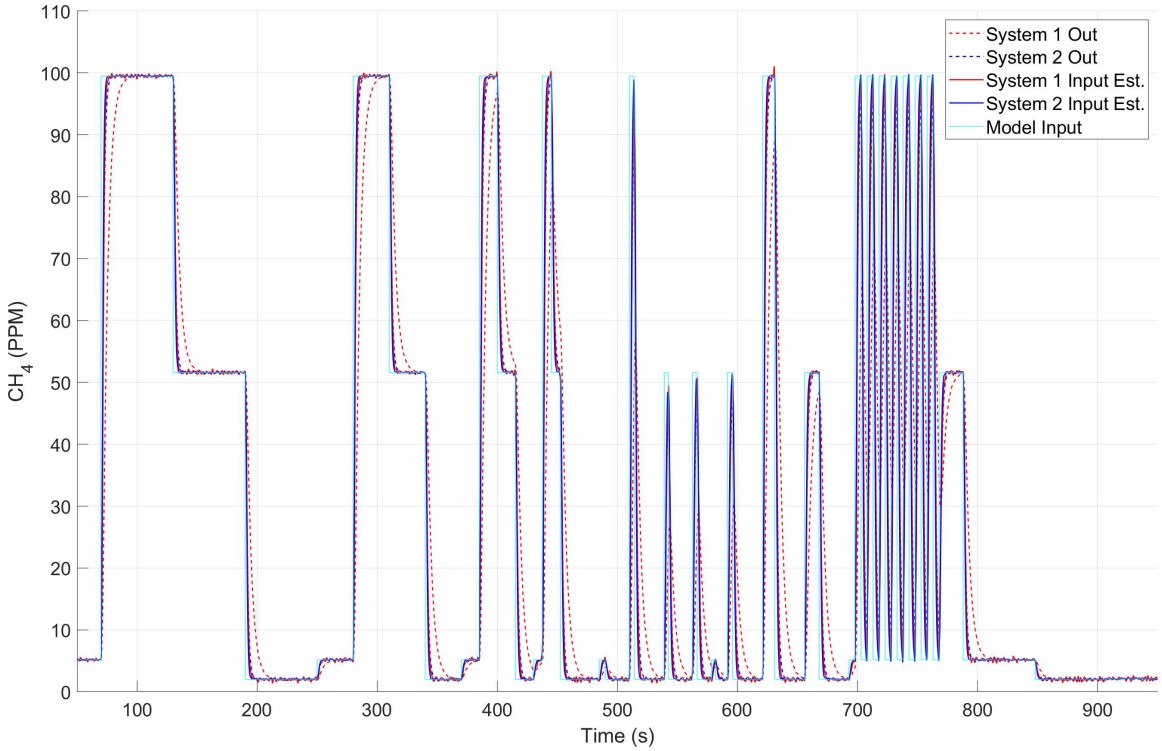

Figure 7. Simulated responses with added random noise and corresponding input estimations. No significant changes in the estimated output were produced.

that noise will be amplified by the input estimation methodology. Nevertheless, much of this noise can be reduced by applying a moving average to the data.

Of course, real ambient gas concentrations don't take the shape of an exact step function. In field data, gas concentrations are seen as spikes that deviate from the natural background concentration of methane. As previously discussed, depending on the exact nature of the leak, along with the ambient weather conditions and the sensing vehicles distance from the leak, these peaks may only be less than a few PPM higher than the background concentration. Occasionally, the peaks can be tens of PPM higher than background. Therefore, it is important to verify the robustness of the input verification methodology with realistic input data. To accomplish this objective, code was written to simulate realistic gas signals. The code allows customizable windows to be specified, where the signal can vary randomly from specified maximum and minimum values. This code allows the creation of signals that can be remarkably similar to the signals seen in field data. An example of such a signal, along with the simulated system responses and input estimations, can be seen in Figure 8. This figure demonstrates the effects that instrument response time can have on field measurements obtained by separate instruments with different response times. By applying the input estimation regime, the differences in the measurements are significantly reduced, and the peak values and waveform shapes are more representative of the true input.

During the analysis of the randomly generated realistic signals, the best value for the damping factor, ζ, was observed to be less than the original ζ value determined for the characterization protocol. A lower ζ means there is less noise artifact to correct for. Since the abrupt step characteristics (discontinuity in slope) within the test protocol are rather extreme, it makes sense that the protocol tends to generate more noise. Likewise, the characteristics of other signals, natural or otherwise, can produce varying amounts of artificial noise. To accommodate this variation, an adjusted ζ value can be obtained for every novel input signal by incrementally lowering the ζ from an arbitrary point and

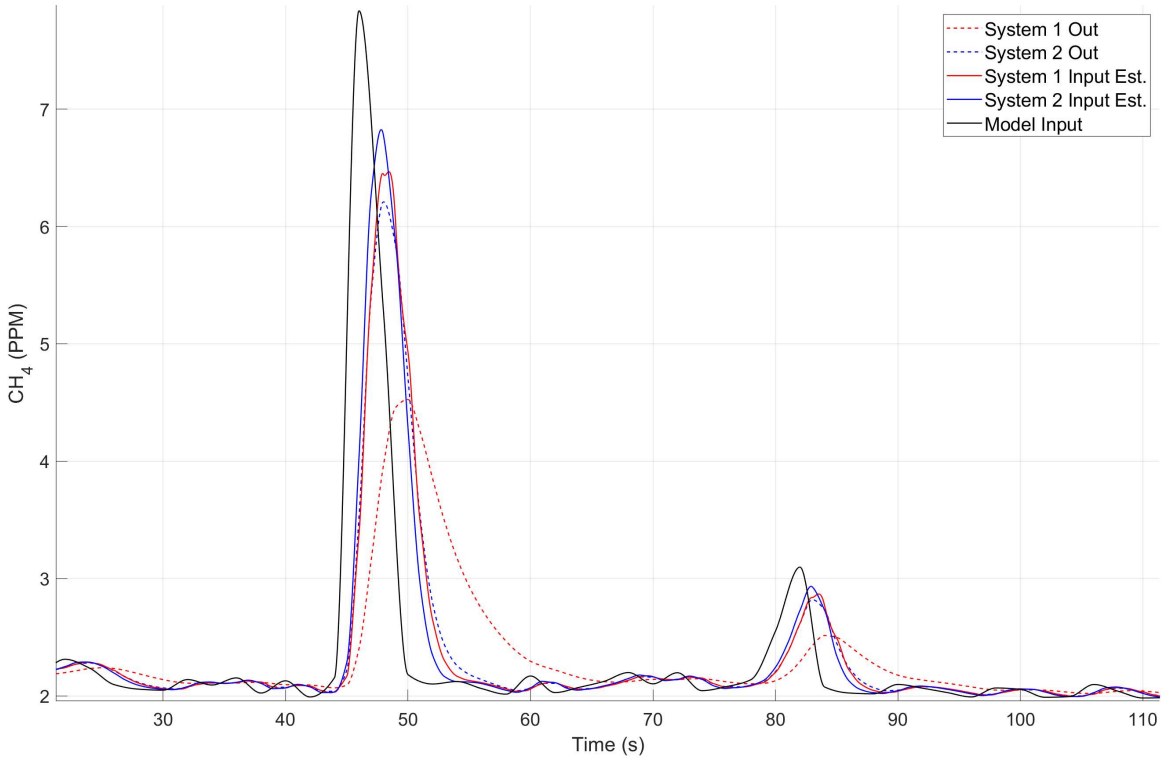

Figure 8. Randomly generated simulated field data with corresponding system responses. Input estimations have peak values and waveform shapes that are more representative of the true input.

analyzing the characteristics of the generated input estimation. If the newly generated input estimation begins to produce points that are below the true input signal, the minimum acceptable value of ζ is reached. The results of such an adjustment can be seen in Figure 9. While the peak values determined with the adjusted ζ are closer to the true peak values, the beginnings of noise artifacts can be seen around the 127 s mark. This behavior motivated development of a more robust and controlled laboratory experiment to determine an optimum ζ as discussed in a later section.

As a final consideration, the finite difference method used by Arieli and Van Liew and Wong et al. [14, 15] was implemented for comparison. For presentation clarity, this approach was only applied to system 1. This comparison can be seen for the square-wave section of the test protocol in Figure 10. The finite difference and Laplace results are similar, and some of the small differences can be attributed to

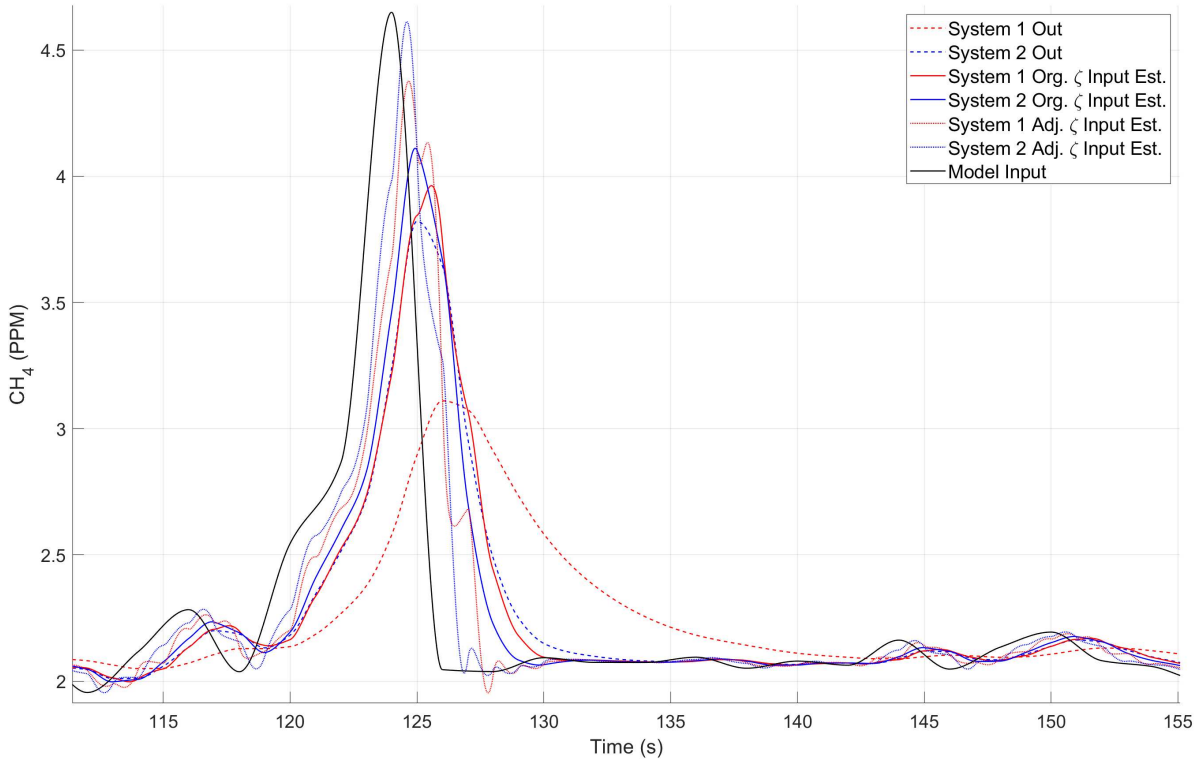

Figure 9. Randomly generated signal with system responses and input estimations based on the original and adjusted ζ values; adjusted ζ values yield improved predictions of maxima but introduce some noise artifacts.

the different approximation values used in the finite difference approach. This similarity in results makes sense, as both methods are mathematically valid, with Laplace transforms simply being an often-easier way to solve differential equations. The finite difference method approach used here requires the first and second derivatives of the output signal to be solved for, either numerically or symbolically. However, the finite difference method is calculated iteratively, and involves the use of loops, as well as the use of two approximation factors (as opposed to the single value, β, used in the analysis discussed in this paper). The ease of use of the Laplace method can be highly advantageous, especially when complex models are involved.

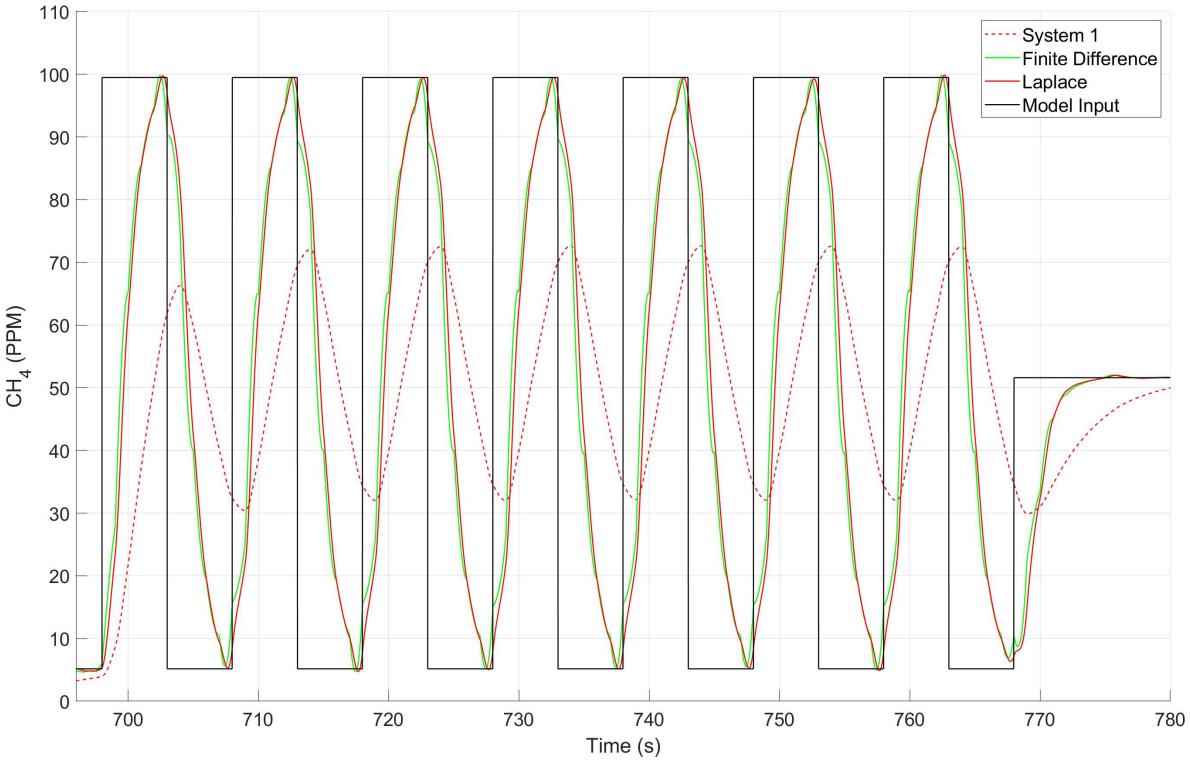

Figure 10. Comparison of Laplace and Finite Difference Methods for the input estimation of arbitrary system 1, focused on the square-wave section. Both methods produce similar results.

Experimental Procedure

In order to apply the input estimation methodology to real-world instruments, an instrument characterization experimental procedure was developed. The testing instrumentation consists of several compressed gas cylinders with a variety of methane gas concentrations connected to two gas manifolds. The methane concentrations that flow into each manifold are controlled by an Arduino microcontroller, as depicted in Figure 11. Mass flow controllers (MFCs) are installed in each gas line upstream of the manifolds. With the addition of MFCS, and because the manifold allows for multiple valves to be opened at the same time, a known mixture in between two gas concentrations can be created. In this experiment, a concentration of 100 PPM is created by mixing the air (0 PPM) and 500

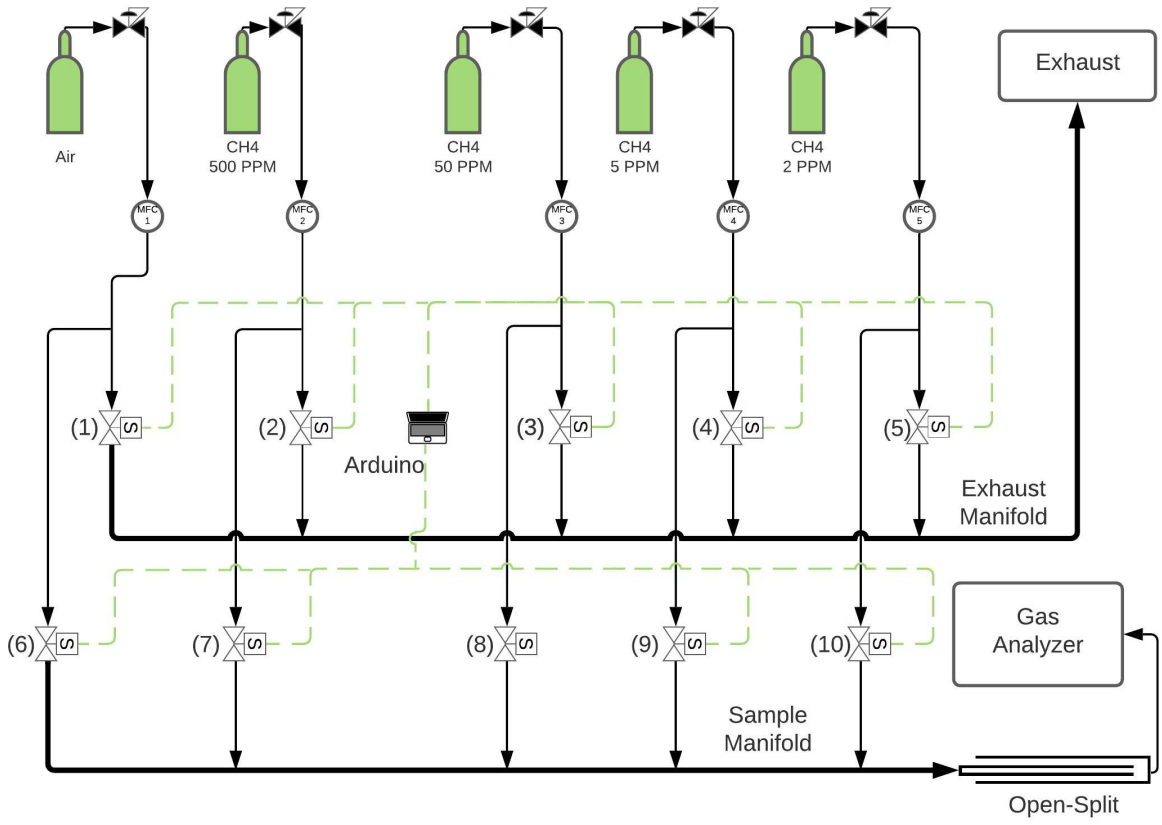

Figure 11. Process flow diagram of laboratory setup for instrument characterization procedure.

PPM canisters using appropriate settings on MFCs 1 and 2 to achieve this concentration. All mass flow controllers, or combinations of flow controllers, are set so that the total flow rate is always constant. For this experiment, a total flow rate of 5 SLPM was selected. Because MFCs have time constants of their own, the experiment was set up so that a continuous, steady flow state is achieved for all MFCs. This is accomplished by utilizing one manifold as an exhaust, controlled by solenoid valves 1 through 5, and one as the sampling line, controlled by valves 6 through 10. The exhaust manifold opens and closes its valve opposite to that of the sampling manifold, so that if valve 6 opens, valve 1 closes, and so on. This strategy results in a steady and constant flow system, eliminating any effects associated with the time response characteristics of the mass flow controllers.

An output tube ran from the sampling manifold to a laboratory fume hood. This line is then connected to an 'open-split'. An open split is a device that prevents over-pressurization of the system by using concentric tubes, where one end of the device is open to the atmosphere – similar in concept to a split injector system for a gas chromatograph. Finally, the instrument being characterized is downstream of the open-split. Each instrument has its own pumping system designed to draw in gas samples from the ambient or in this case from the open split.

The test itself is programmed on the Arduino using the C coding language. The code for the test consists of a simple array, denoting which valves should be open and for how long. The array allows for the test protocols to be easily modified for the desired response characteristics. This experimental setup allows the test protocol shown in Figure 1 to be applied to the instrument being characterized. The range of gas values were selected to cover the specified operational range of the LGR instrument, which has a recommended maximum methane input concentration of 100 PPM. All instruments were characterized individually using this experimental setup.

Characterization Analysis

The analysis of the data acquired during the characterization experiments has been performed within MATLAB. The data files contain the concentration readings and the associated time stamps. All the instruments have an average data sampling rate of 1Hz, however the true time difference between each measurement is not exactly 1.0 s, and instead fluctuates by tens of milliseconds. Therefore, for the most accurate model to be developed, it is important to use the actual time stamp values recorded by the instrument for each data point, instead of assuming uniform 1Hz data. Additionally, the data are interpolated using a piecewise cubic function to 100Hz within MATLAB before characterization.

The actual parametrization process of the instruments is an automated process that is done within MATLAB's System Identification Toolbox. This software is designed to analyze input-output systems and can model them with various techniques. The modelling software only requires the input and the output of the system – all other values, such as time constant and delays (the time difference from the start of the input to the start of the response) are determined within the analysis. However, due to the limitations of the Arduino-controlled manifold, the state of the valves is not recorded with time. This issue is easily overcome by applying the same testing protocol, previously described in the analytical verification section, and shown in Figure 1, within MATLAB. This approach means that the true delay of the testing system is not necessarily determined, but this limitation is not an issue, as the delay value does not affect the actual time response characteristics. Additionally, the delay will change with any configuration that these instruments may be installed in, while the time response characteristics will not.

Instrument calibration does pose a challenge during the testing procedure. An incorrect instrument calibration results in steady-state readings that are different than the true value. For instance, the Aeris unit was observed to report a steady-state value of approximately 93 PPM for a true gas concentration of 100 PPM. While the Aeris software allows for recalibration, and a gain parameter

could be added to the transfer function as a calibration correction, this instrument had previously been used to record natural gas survey data with its current calibration. Therefore, it was determined that a recalibration of the instrument was not desired for existing data sets. Additionally, the purpose of the research in this paper is to characterize the instrument response time characteristics, which is separate from the calibration of these instruments. If a gain parameter were to be used as a calibration factor, this factor would need to be recalculated for each instrument in order to accommodate each specific instrument's calibration. Additionally, some instruments, such as the Heath, do not allow for a manual calibration. Therefore, to model the instruments covered in this paper without performing a calibration, the gas concentrations for the input in MATLAB for each instrument were adjusted to the steady-state values achieved by these instruments. For the Aeris, this adjustment can be seen in Figure 12.

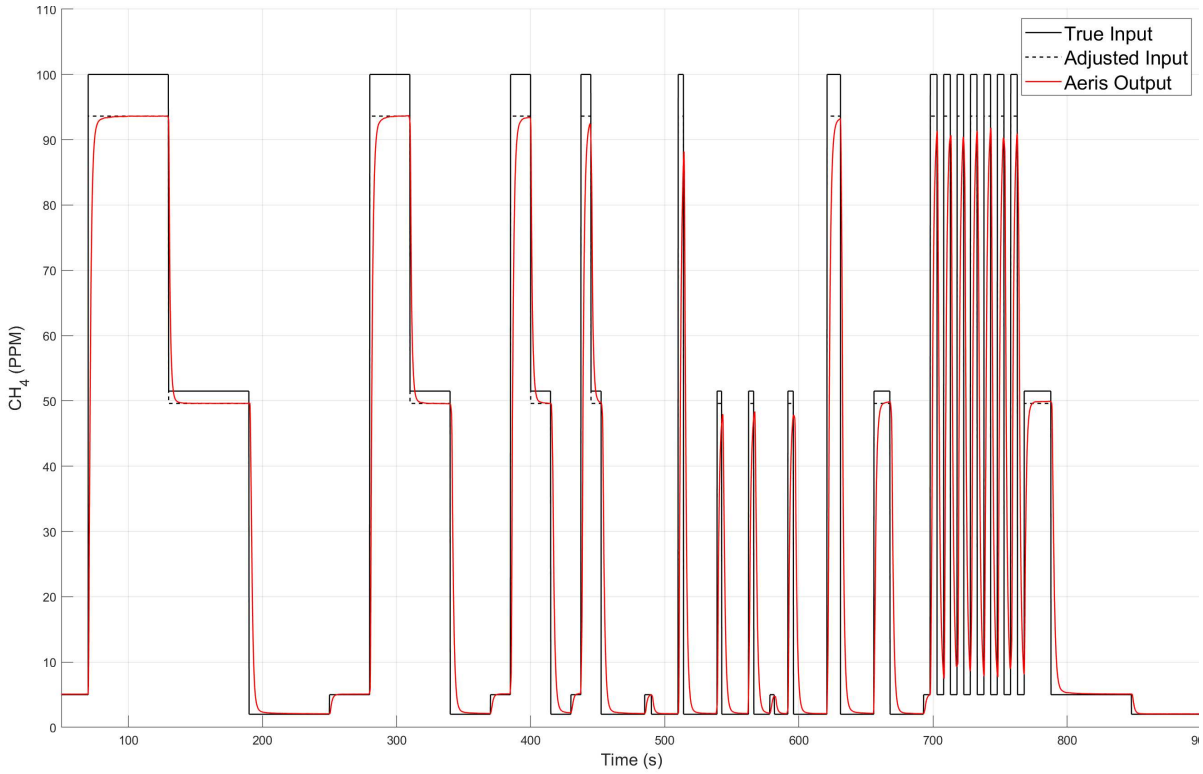

Figure 12. Aeris response to the test protocol, showing the true and calibration-adjusted inputs.

As discussed, a three-time-constant system is used to model the instrument response characteristics. With the test input coded to reproduce the instrument characterization protocol of Figure 1, MATLAB runs through a series of iterations to determine the time constant values of each instrument based on the recorded instrument response data. If needed, the bounds for the time constant values can be changed and the iteration process can be repeated. Each time a value is changed, or another iteration process is run, MATLAB will record the values calculated as individual models. These models can then be compared to the recorded instrument response data, with correlation values displayed. Eventually, a maximum correlation value is reached, and the corresponding time constant values are used as the basis for the model in further analyses. Comparisons of four of the generated models for the Aeris Pico unit are shown in Figure 13 with the corresponding correlation values shown in the legend. The resulting time constants of the instruments as determined by this procedure are listed in

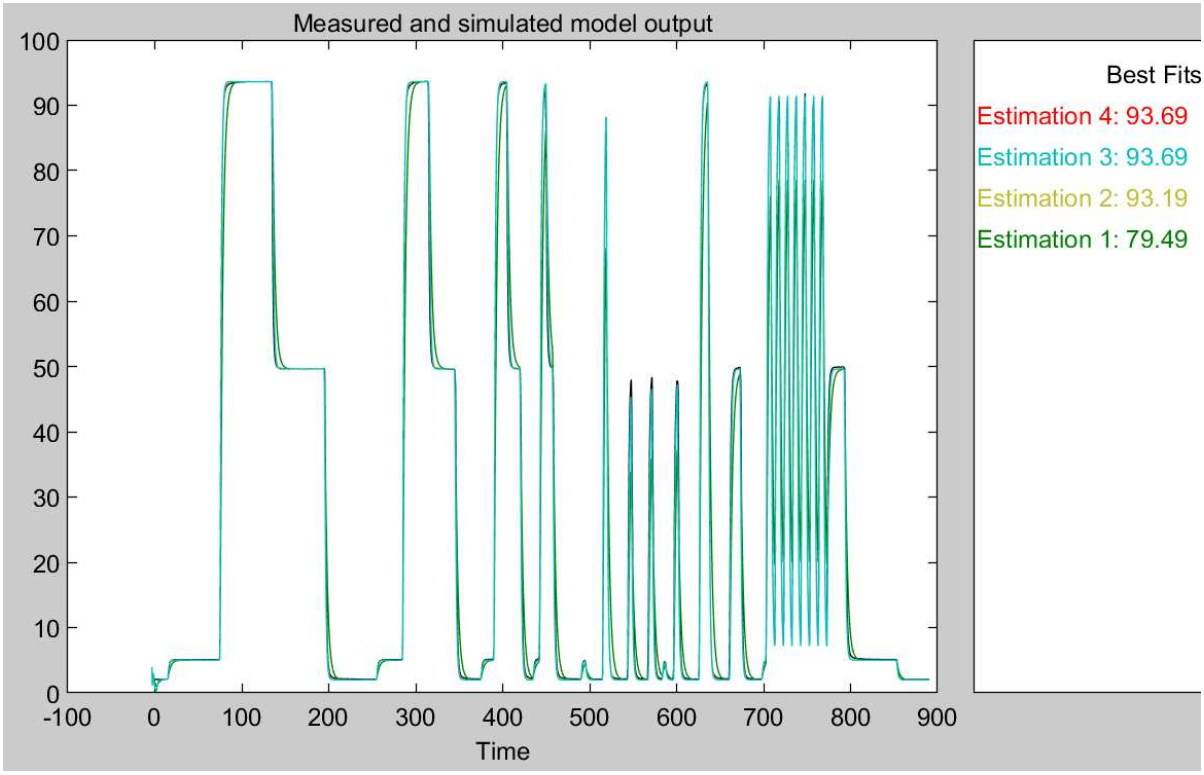

Figure 13. A comparison of the various models that were estimated within MATLAB for the Aeris Pico unit, showing how well each model fits the output data and the corresponding correlation values.

Table 1 along with each instrument's pump flow rate. Additionally, the pump mass flow rate of each instrument was measured in SLPM using a mass flow controller. It is interesting to note that, as the pump speed of the instrument increases, the time constants decrease, which is to be expected.

The results of the characterization experiments are shown in Figure 14. The differences in calibration, as well as the recorded instrument response, can clearly be seen in Figure 14 (a). In this experiment, the Aeris and LGR instruments are clearly the most accurate. The Heath instrument displays quite a bit of noise, which is due to several factors. While the Heath instrument has a fast pump rate and response characteristics, it also has low concentration resolution, only reporting gas concentrations as whole ppm values. Consequently, there appear to be concentration jumps during sections of otherwise steady-state readings. Additionally, the Heath significantly underreports the true gas concentrations,

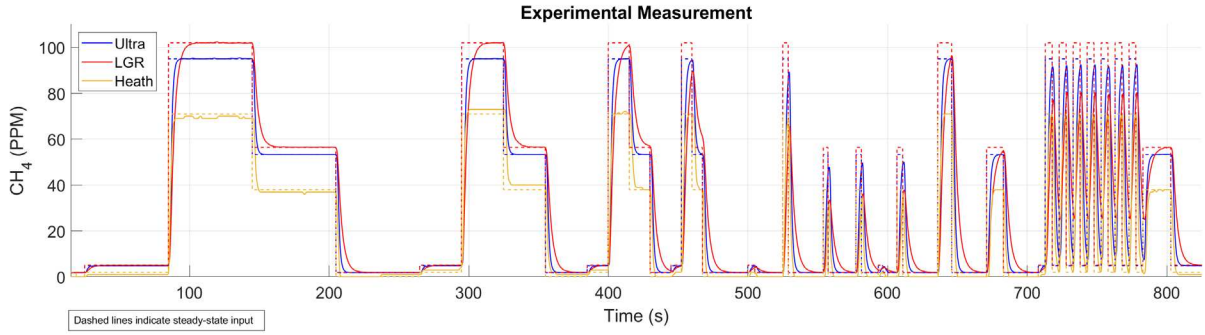

(a) Experimental measurements

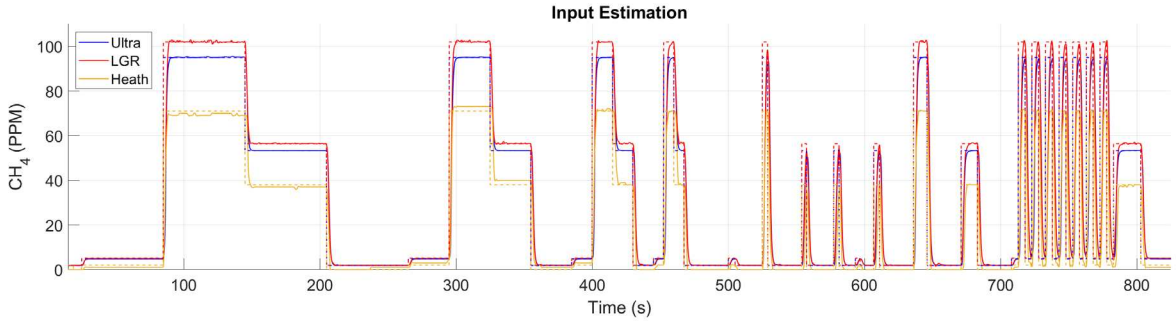

(b) Input estimations

Figure 14. Experimental measurements (a) and input estimations (b) resulting from the instrument characterization procedure for three instruments. Dashed lines represent calibration-adjusted input signal for each instrument.

only reporting values of around 65 PPM for the 100 PPM gas flow. Furthermore, the Heath is most inaccurate at low concentrations, causing the 5 PPM and 2 PPM sections to be almost indistinguishable. Because of these factors, the model developed for the Heath instrument is the least accurate of the three considered here.

The input estimations for all three instruments are presented in Figure 14 (b), with the adjusted true input for each instrument shown with a dashed line. Here, the best value for ζ was determined using the method described in the next section. It is clear that the input waveforms are more accurately reproduced using the input estimation procedure compared to the raw instrument responses. Additionally, the maxima values for the shorter bursts of gas present at the end of the test ($t > 500$ s) are more accurately reproduced compared to the raw instrument output. While all the instrument input estimations can reproduce the maximum and minimum values of the square-wave section ($t > 700$ s), the exact shape of the step is not reproduced. This behavior was predicted in the analytical verification section and as discussed, reproducing the exact shape of the step is not viewed to be as critical as achieving the maximum and minimum values that exist in the signal. The input signal used in the testing protocol would not exist in nature, however a well-defined test protocol like this is required to accurately determine the time response characteristics of the instruments. This is why the randomly generated "natural" signals and simulations were created to verify the methods used in this analysis. Unfortunately, it is not possible to experimentally reproduce a natural signal while also knowing the true gas concentration at the inlet of the instruments. Nevertheless, the benefits of the of this input estimation procedure can be seen in this experiment, especially with the LGR instrument. The time constants of the instruments are listed in Table 1. Of the three instruments, the LGR has the slowest time response characteristics. Again, this is most notable during the square-wave section, where the slow response characteristics of the LGR instrument cause the response signal to resemble a sinusoidal wave with an amplitude much less than that of the true input signal. Nevertheless, the input estimation

Table 1 – Time constants and pump flow rates of the gas analysis instruments.

Instrument	$\boldsymbol{\tau_1}$ (s)	$\boldsymbol{\tau_2}$ (s)	$\boldsymbol{\tau_3}$ (s)	**Pump Flow Rate (SLPM)**
Aeris Pico	0.329	0.342	1.106	0.78
Aeris Ultra	0.372	0.372	1.096	0.78
LGR	0.509	0.509	2.997	0.45
Heath	0.681	0.036	0.681	1.5

for the LGR is still able to resolve the maximum and minimum values of the square wave. The two Aeris units have nearly the same time constants. This is not a surprise, as the only stated difference between the two is that the Ultra has more advanced thermal insulation in the sensing cavity, with the laser and pump systems purported to be the same. Therefore, the two instruments reproducing the same values can be considered an example of the reproducibility of the time constants between two separate models of the same instrument. For this reason, the Ultra will be the only Aeris instrument considered in further analysis.

Zeta Calibration

As previously discussed, while the instruments themselves are characterized by time constants, the input estimation regime requires a damping value, known as ζ. It was shown the best value for ζ can change depending on the response characteristics of the instrument. In the analytical procedure, the effects of altering the ζ value can be directly compared to the true input signal. However, with real-world data, the true input signal is not known. It was theorized that the zeta value could be lowered until the estimated input signal began generating points below the minimum value of the reported gas concentrations, since this value would most likely be the natural background concentration. However, when this method was applied to real-world results, a wide range of ζ values was calculated for a single

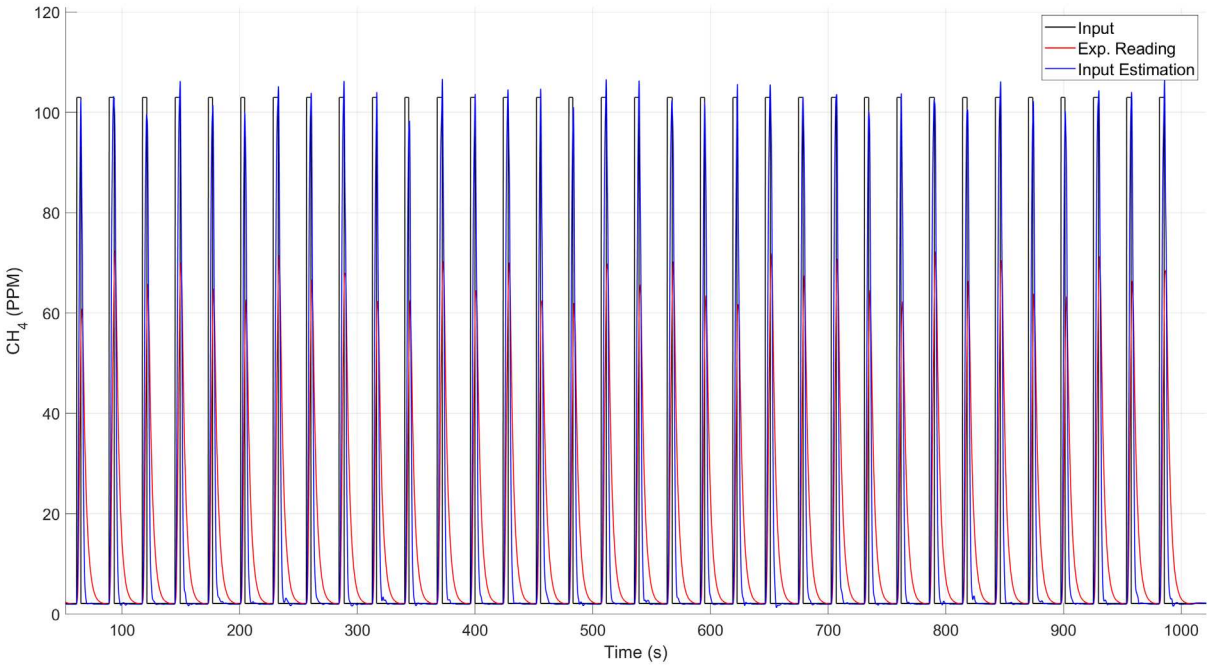

Figure 15. Zeta calibration procedure applied to the LGR instrument. Input estimation with optimum zeta yields a mean peak value equal to the known input concentration.

instrument, whereas a method that yielded a more consistent ζ value was needed. Additionally, some noise was produced with this method. Therefore, a laboratory test was developed to determine a well-defined zeta value applicable to a wide range of conditions.

By subjecting an instrument to bursts of a single gas, with the duration of the burst varying, a variety of peak shapes was generated. Varying burst durations were used in order to better represent real-world data. Since only the length of the burst is varying, the true input to the instrument is each instrument's steady-state reading of that gas. When an optimal ζ value is achieved, the input estimation regime should produce a signal for which the average value of the peaks is equal to the instrument's steady-state reading. Consistent with the original concept of finding the optimum ζ value, ζ is lowered incrementally until this average is reached. From this point on, ζ is held constant for all further analyses. The results of this test performed on the LGR instrument are presented in Figure 15 with a detailed view shown in Figure 16. While the estimation results in some peaks that lie above the true input

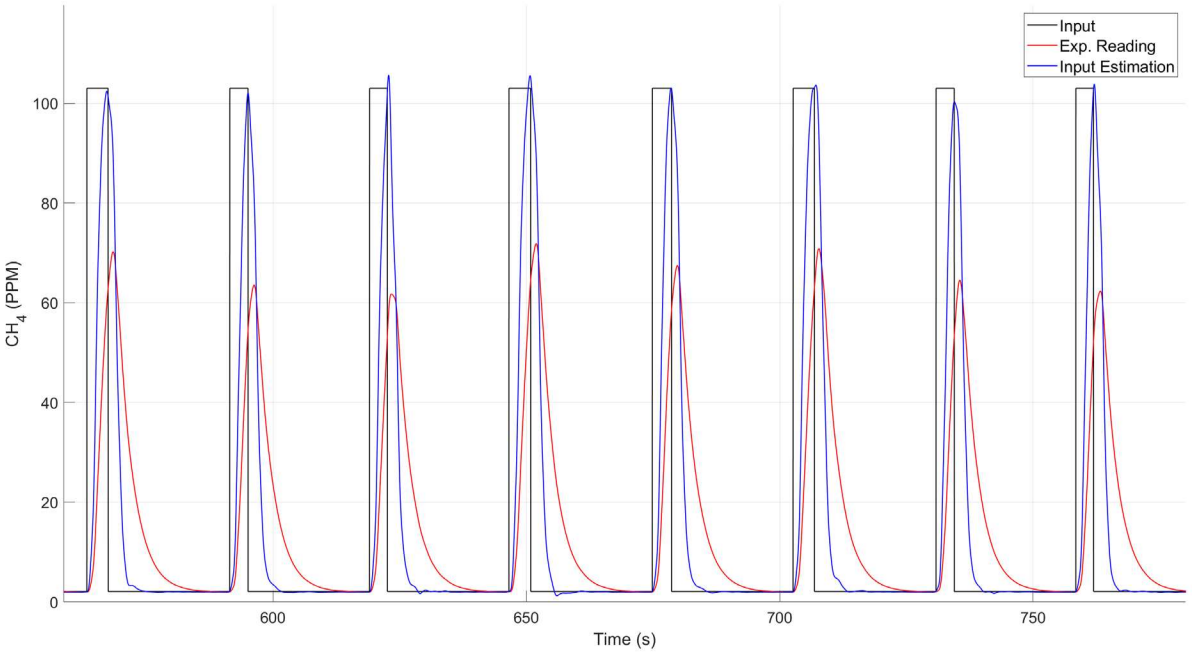

Figure 16. Detail of zeta calibration procedure, applied to the LGR instrument. Input estimation with optimum zeta yields a mean peak value equal to the known input concentration.

concentration and some that lie below the true input concentration (due to the limited data sampling rate), the average value of these peaks is equal to the known input concentration. With real-world data, the length of time the gas is detected can have just as much of an impact on the peak geometries and maxima as the true concentration can. For this reason, a ζ value that achieves an average output equal to the true input can be considered a reasonable approach. The effect of ζ value on the LGR mean peak value is plotted in Figure 17. The intersection of the dotted lines in this figure represents the optimum ζ value for the LGR. Results of this calibration are listed in Table 2 for the three instruments. It is interesting to note that, as instrument response time increase, the value for ζ also increases.

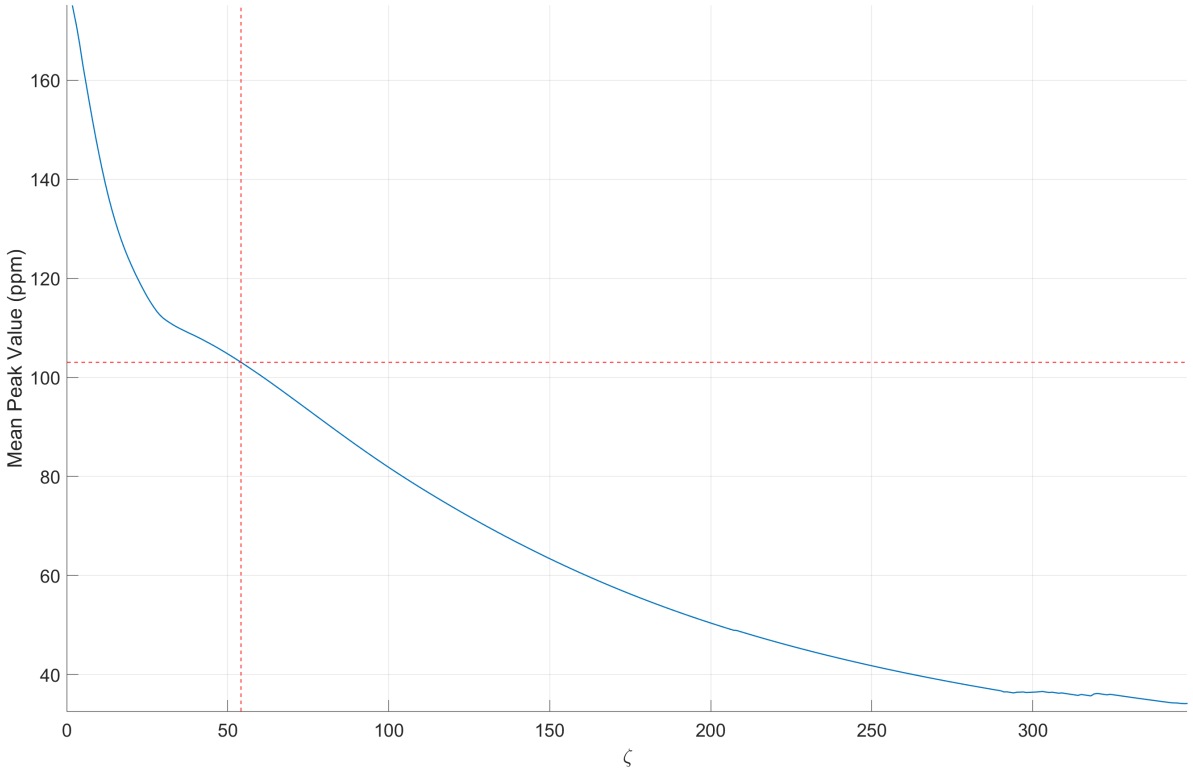

Figure 17. Effect of ζ value on the mean peak estimation from the burst tests. Horizontal red line indicates the LGR's steady-state value for the gas, with the vertical red line representing the corresponding optimized ζ value.

Table 2 – Zeta values of the gas analysis instruments.

Instrument	***ζ***
Aeris Ultra	50.1
LGR	54.3
Heath	40.56

Fume Hood Testing

Once the instruments were characterized, a test was developed to compare the effects of the input estimation when the gas input is unknown. For this test, two instruments were plumbed in parallel, so that the instruments are sampling from the same air stream. The instruments are then placed in the fume hood, and the gas inlet line is placed a short distance away from the inlet of the instruments, as shown in Figure 18. This arrangement allows the gas to be randomly mixed inside the fume hood, simulating the kinds of signals that are observed in the field. Since the true time-dependent inlet concentration at the instruments is unknown, the goal of this experiment is to use the input estimation procedure to remove the differences between the output signals generated by the two instruments. Again, while the use of this input estimation should, in theory, generate an output signal closer to the true value, it is not possible to know the true gas concentration values in the field. Since instruments with different response times will generate different signals from the same input, the goal is instead to remove these differences and thus minimize data collection ambiguities between different gas analyzing instruments.

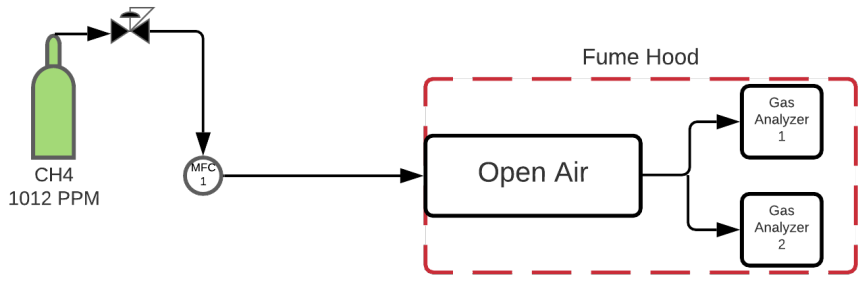

Figure 18. Process flow diagram for fume hood test allowing the gas to be randomly mixed inside the fume hood, simulating the kinds of signals that are observed in the field.

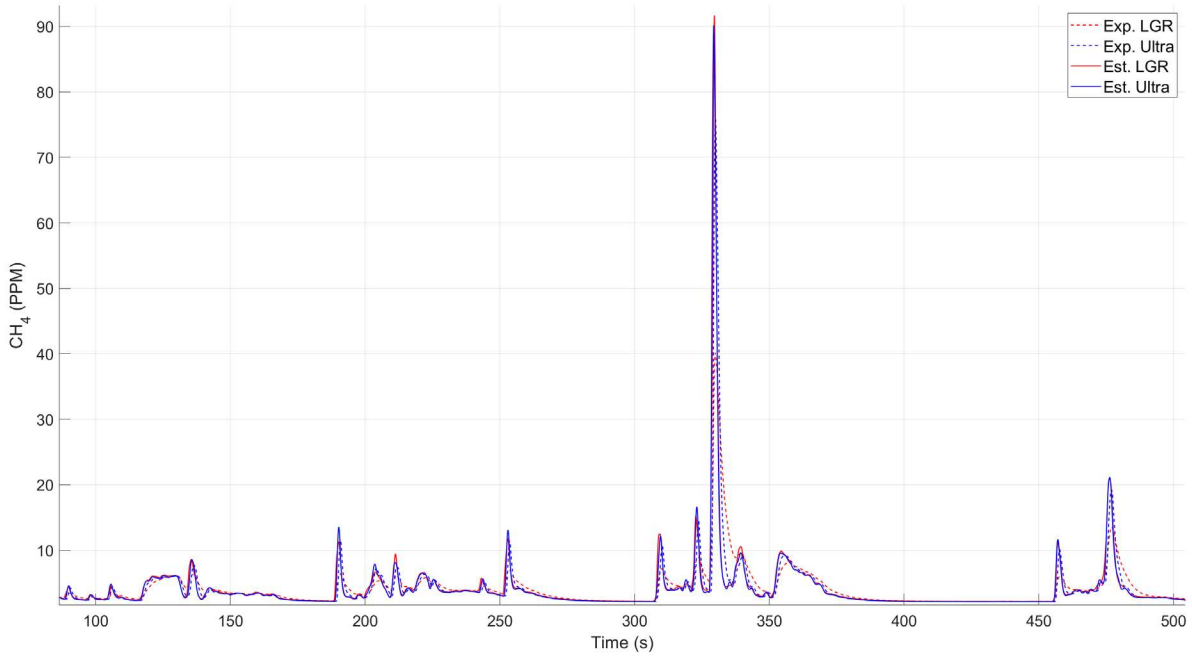

Figure 19. Fume hood test data, showing the original and corrected signals from the LGR and Ultra instruments; corrected input estimation signals are very similar.

An example of one of the data sets obtained with fume hood test is shown in Figure 19. Here, the fume hood test is run with the LGR and Ultra instruments plumbed in parallel. The measured signals clearly resemble some of the random signals seen in the analytical section of this paper, as well as the signals that are seen in actual field research. In this particular test, some higher peaks were generated, but many peaks are only slightly above the natural background concentration. A variety of peak geometries is a common occurrence in survey data, so the fume hood testing replicates these characteristics well. The effects of the time responses of the two instruments can clearly be seen, with the Ultra reporting higher values and sharper peaks in the raw, uncorrected data. This makes sense, as the Ultra has been shown to have a faster time response than the LGR. However, once the input estimation regime is applied, the two corrected input estimation signals are very similar.

While one can simply observe the generated plots and see that the methodology brings the two signals closer together, an analytical approach is required to quantify their similarity. There exist a variety of methods to compare the various output signals. One simple method is to find the Pearson

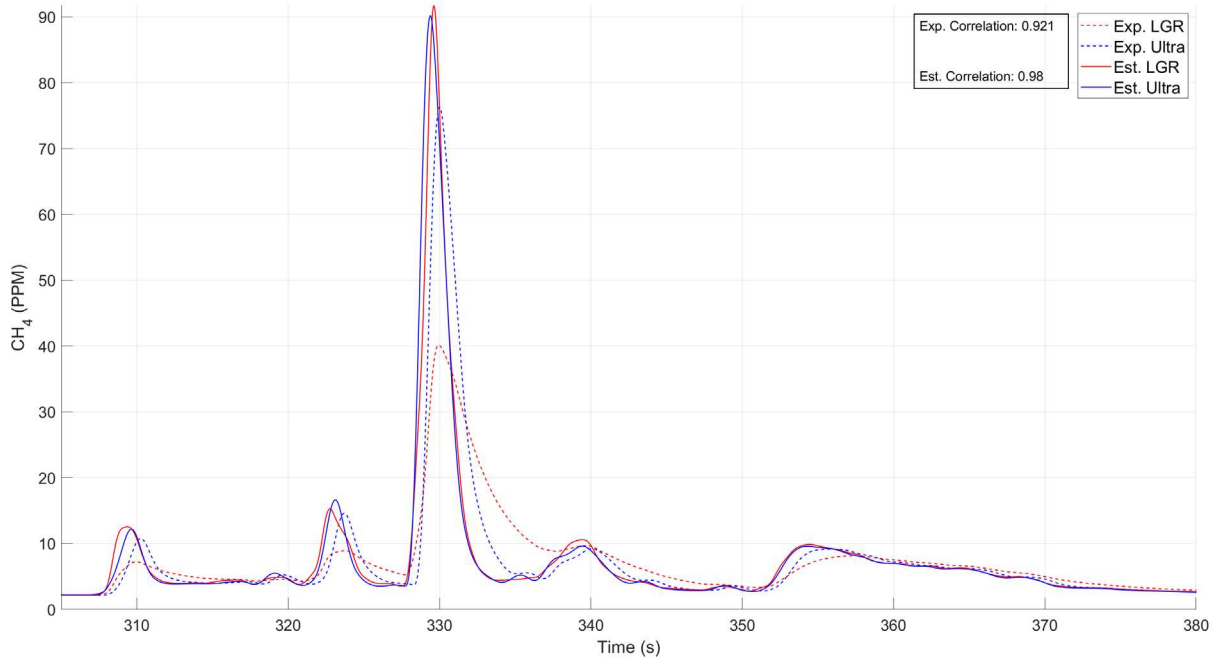

Figure 20. Detail of fume hood test data, showing the original and corrected signals from the LGR and Ultra instruments. The PCC values, as calculated from the data within the displayed range, show improved correlation for input estimation signals.

correlation coefficient (PCC) between the two pairs of signals. To achieve a fair comparison between the two signals with this method, only regions where actual peaks are detected are considered – if this comparison was done on the entire data set, an artificially high correlation value would be produced, since the regions where only the background concentration is detected by the two instruments dominate the data set. Still, even when only considering a peak region, the original signals have reasonably high correlation values. A small subset of peaks from the data set in Figure 19 is shown in Figure 20, with the experimental and estimation values of the PCC shown. Even when considering this smaller region, PCC values do rise, but only from 0.921 to 0.98 because many of the data points represent background CH4 which the two instruments detect similarly.

While PCC is a useful tool to estimate the similarity between the signals, it doesn't provide any detail on why the signals are similar. As discussed, maximum peak values are a commonly used parameter in analysis of leak survey data. Peak widths can also be a useful characterization parameter.

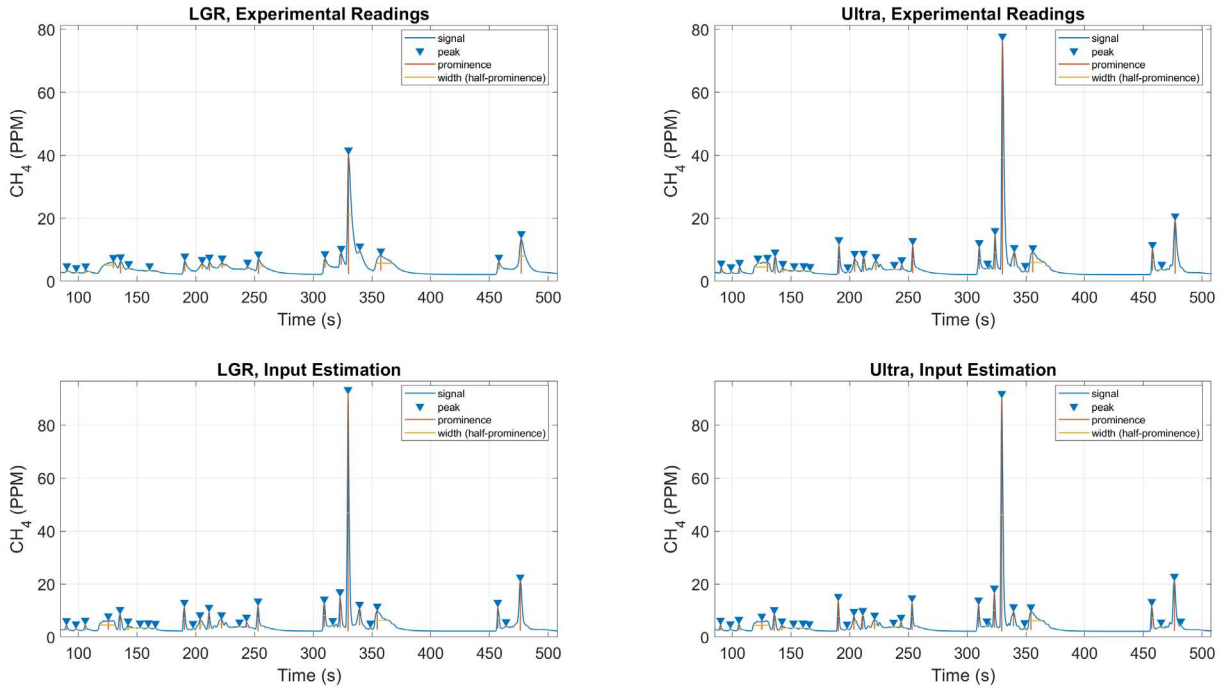

Figure 21. Peak analysis of the fume hood test data, experimental readings and input estimations. Note the improved similarity between the LGR and the Ultra signals after application of the input estimation procedure

Both of these parameters are strongly influenced by the instrument's response characteristics. To that end, analysis is performed to locate and characterize all local measurement peaks contained within a signal. This analysis provides useful information such as the peak's location in time, its width, and the maximum value achieved. By comparing these features, along with the total number of peaks located, the instruments can be compared in a way that is much more applicable to the overall scope of methane mapping research.

Figure 21 shows an analysis of the peaks observed within the fume hood data set. The graphs in the top row of the figure show this analysis when applied to the raw experimental readings, with the bottom row showing the peak analysis when applied to the same signal generated from the input estimation procedure. Note the improved similarity between the LGR and the Ultra signals after application of the input estimation procedure. Peaks are marked with an inverted triangle symbol. Each peak is characterized by its maximum value, its prominence, and its width. Prominence is a

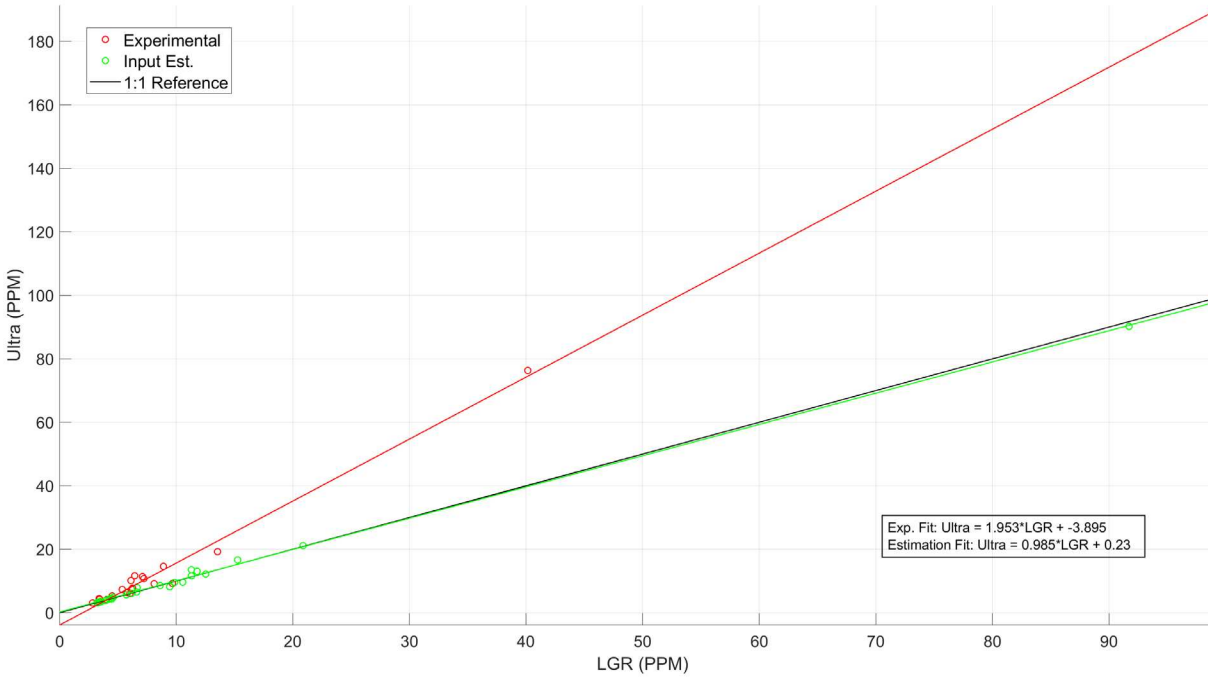

Figure 22. Scatter plot of the fume hood peak data, demonstrating the higher agreement between sensors post-correction; the input estimation values associated with the two instruments correspond nearly one-to-one, with a near-zero intercept.

measurement of the peak's height relative to other peaks. It is found by considering a horizontal line, measured from the peak's maximum. This horizontal line extends from both sides, until it either intersects the signal, or reaches the end of the signal. The minimum values on either side of the peak are then determined, and the prominence is defined as the difference between the peak and the higher value of the two minimum values found. The peak width is then defined as half of the height of the prominence. In total, this analysis provides a variety of useful characteristics of each peak. Settings can also be applied to determine what qualifies as a peak, such as minimum width, minimum height, minimum prominence, and minimum distance from another peak.

A direct comparison of the peak values detected by the two instruments is presented in Figure 22. This plot shows the value read by the LGR on the x-axis and the value, for the same peak, read by the Ultra on the y-axis. For perfect maximum peak correlation, all the data points would lie on the black 1:1 line representing $PPM_{Ultra} = PPM_{LGR}$. These peak values are shown for both the experimental readings,

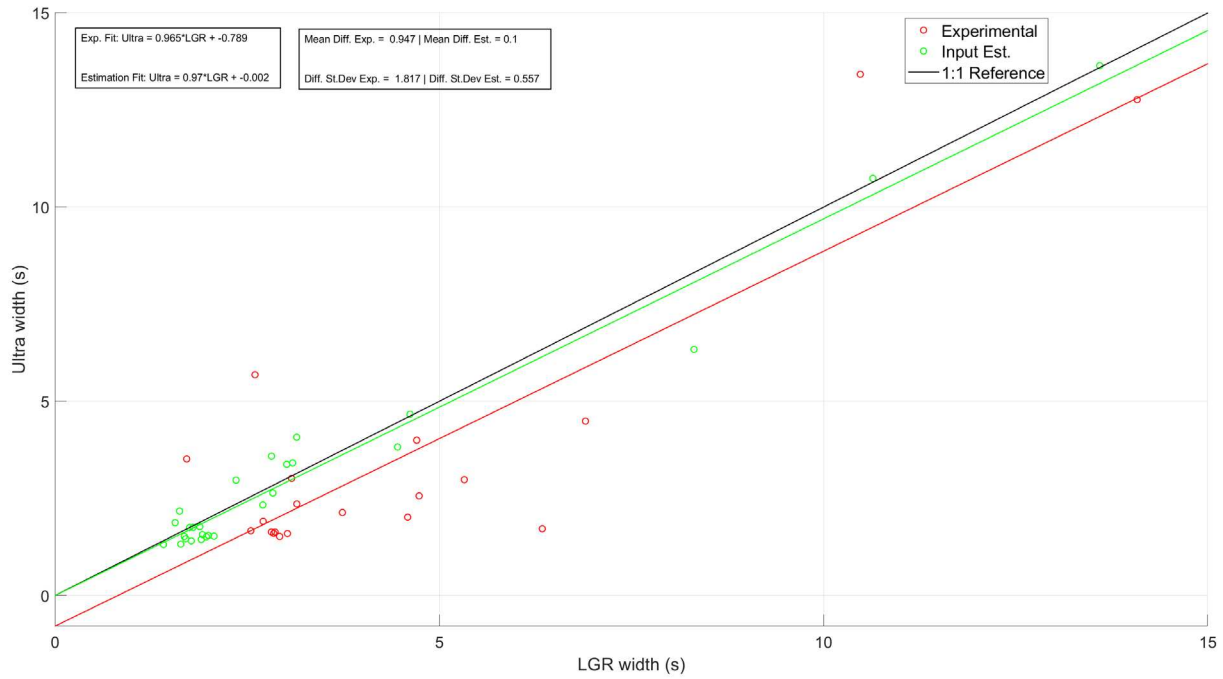

Figure 23. Scatter plot of the fume hood peak-width data, demonstrating the higher agreement between sensors post-correction; mean and standard deviation of the difference between the widths of the two instruments for the input estimations is significantly lower for both values.

and the corresponding outputs after the input estimation regime is performed. For this data set, the raw experimental peak readings of the Ultra are almost twice that of the LGR. Additionally, a negative y-intercept is calculated using the raw data. However, after the input estimation regime is run, the input estimation values associated with the two instruments correspond nearly one-to-one, with a near-zero intercept. By similar methodology, the peak widths in both cases were also analyzed, as shown in Figure 23. While slopes of the results are displayed, the widths of the peaks are not linearly related. However, the mean and standard deviation of the difference between the widths of the two instruments are also shown. The input estimation regime significantly lowers both values, once again demonstrating the stronger agreement between the two instruments after the input estimation regime is considered.

To understand how the slopes of the peak data produced by the LGR and Ultra instruments should compare, an analysis was conducted to compare their steady-state readings for a variety of gas

concentrations. Similar to the field tests, the instruments are plumbed in parallel. The results of this

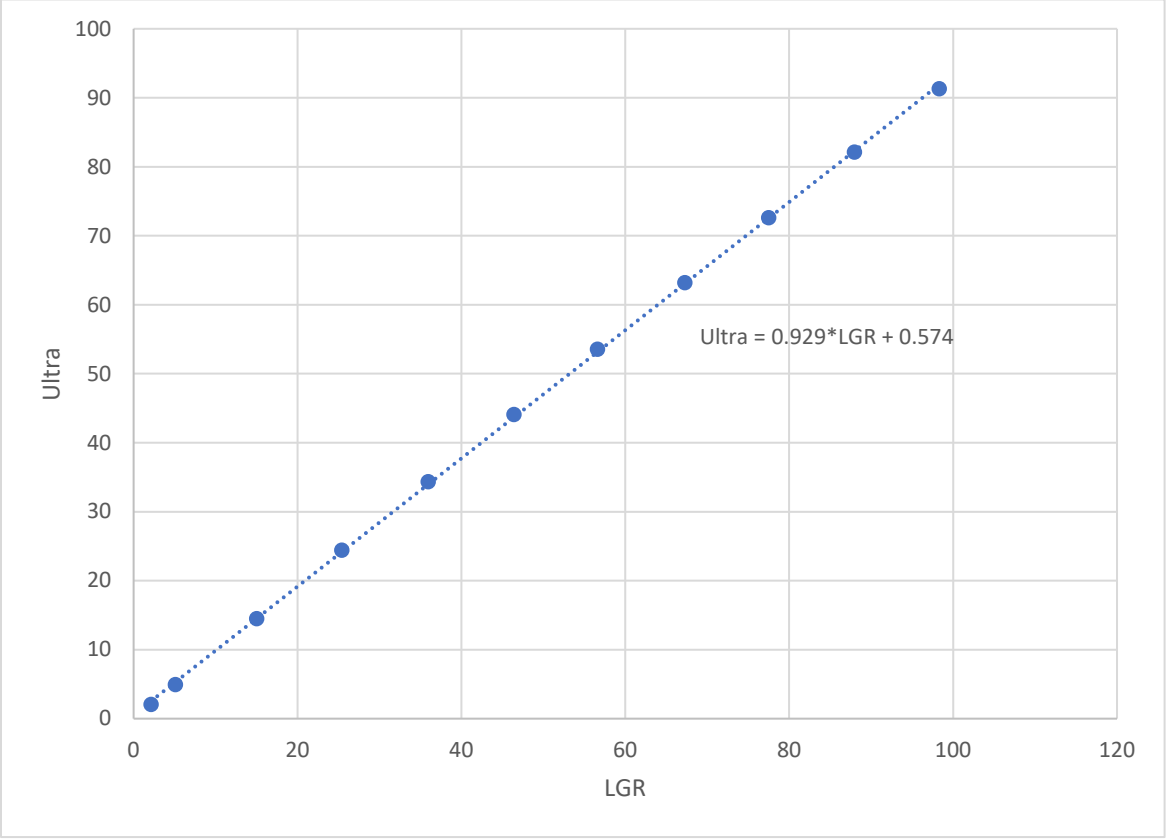

Figure 24. Steady-state reading comparison between the LGR and Ultra instruments with linear fit, consistent with the fact that at steady-state, the Ultra reports approximately 93% of the value reported by the LGR.

comparison are presented in Figure 24. At steady-state, the Ultra reports approximately 93% of the value reported by the LGR. Since the input estimation regime is designed to reproduce the values the instrument would otherwise see at steady-state, it follows that the estimation values of the Ultra should, on average, be lower than the estimation values of the LGR. This is exactly the result that is achieved, for the fume hood test.

Controlled Release Field Test

One component of the methane mapping research has been the utilization of controlled release field testing. This testing involves the release of pure methane and ethane gasses at a variety of flow rates and a variety of locations. During this testing, all components of the overarching research efforts

are applied – the methane mapping vehicle itself, along with all its various data logging instruments, as well as the meteorological data taken from a stationary anemometer array. The goal of this testing is to understand how methane plumes behave in real-world conditions, and how to estimate the size and location of these leaks. The methane mapping vehicle is equipped with an inlet manifold along the length of its front bumper, and a line is plumbed from this manifold to the gas analyzer, which resides in the trunk of the vehicle. During these tests, the vehicle is driven at a variety of speeds and distances from the source of the methane leak. Tests where the vehicle is simply parked downstream of the plume are also conducted; these are known as stationary tests. By varying the methane and ethane flow rates, different leak sizes are simulated during this testing.

For the purposes of the input estimation methodology, two instruments are used, plumbed in parallel on the vehicle, with both connected to the same inlet manifold during the controlled release. Again, this configuration allows both instruments to be analyzing the same gas stream, similar in concept to the fume hood tests. Data were obtained with five different source flow rates: 50, 25, 10, 5, and 2 SLPM. This range of flow rates allows the simulation of both large and small natural gas leaks, resulting in a variety of peak shapes, maximums, and widths. Instrument results from a stationary test, with a release rate of 5 SLPM are shown in Figure 25. By applying the same peak analysis discussed in the fume hood test section, Figures 26 and 27 are produced. While the difference between the raw data acquired with the two instruments isn't as extreme in this release as it was for the fume hood tests (an experimental slope of 1.124 versus the 1.953 slope for the fume hood test), the input estimation regime results in a slope of 0.985, much closer to measured steady-state slope shown in Figure 24.

Results from a controlled release test in which the vehicle was repeatedly driven past the leak, at a variety of speeds and distances, are shown in Figure 28. The peak analysis of the data set is shown in Figure 29. The scatter plot results are shown in Figure 30, with the original slope being 1.558 and the estimation slope being 0.97.

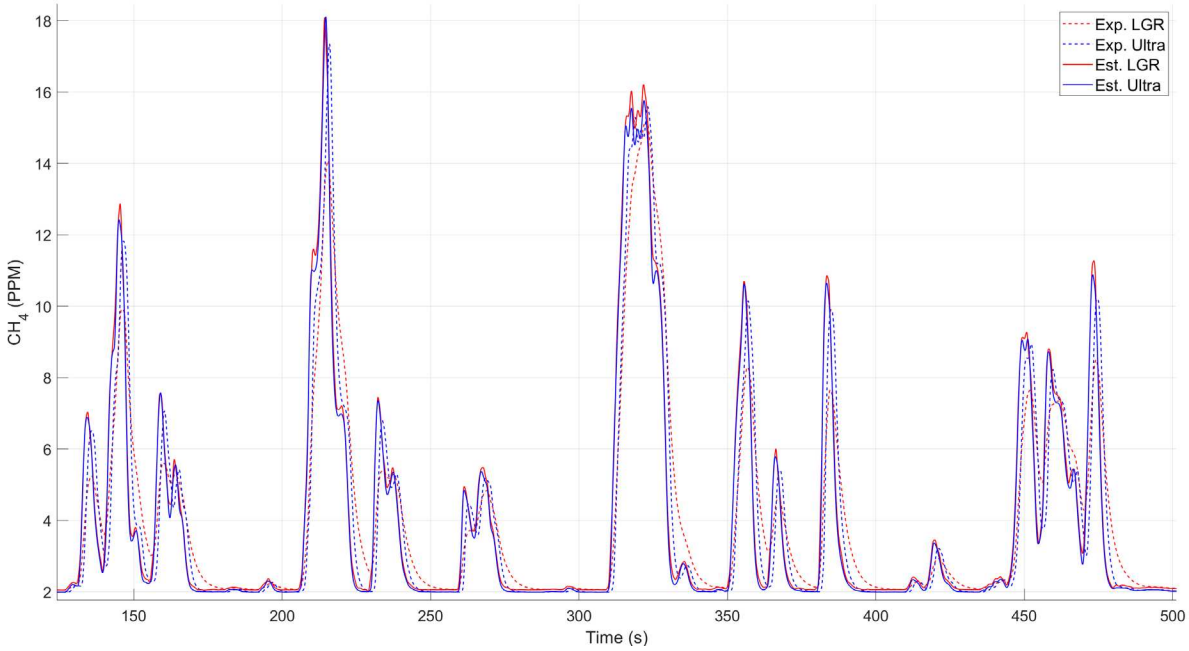

Figure 25. Instrument output and estimation signals from a stationary vehicle, 5 SLPM controlled release. Input estimate produces similar peak values and waveform shapes.

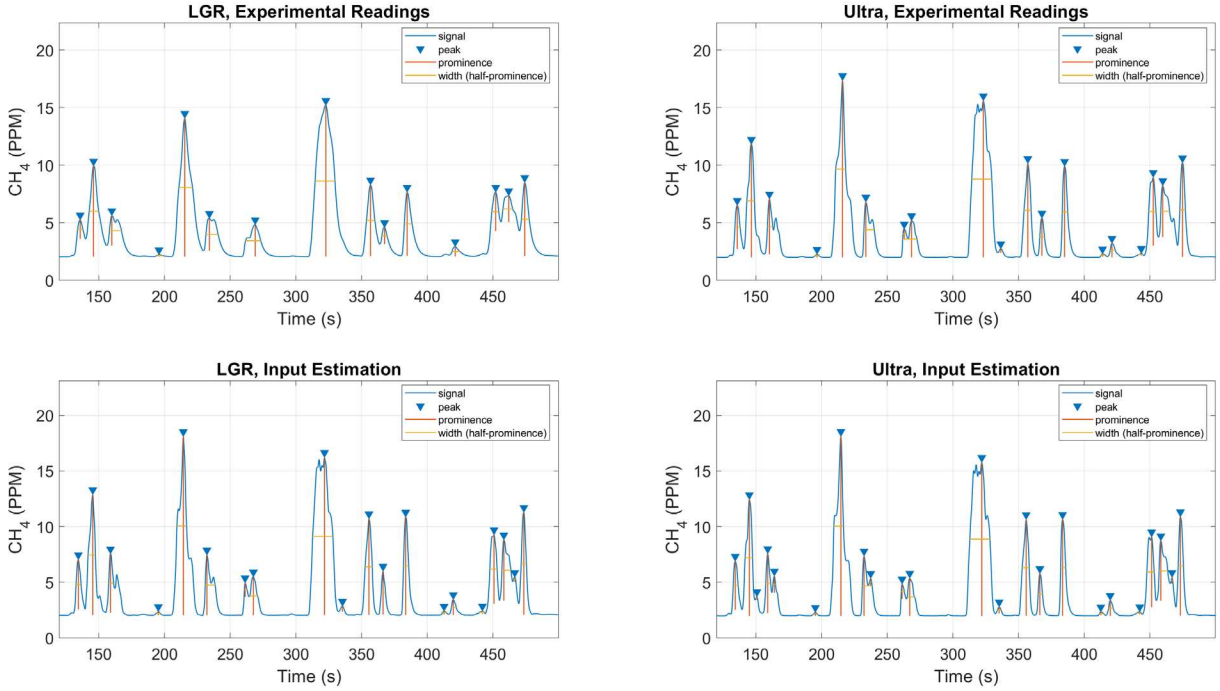

Figure 26. Peak analysis of the stationary, 5 SLPM controlled release. Note the improved similarity between the LGR and the Ultra signals after application of the input estimation procedure.

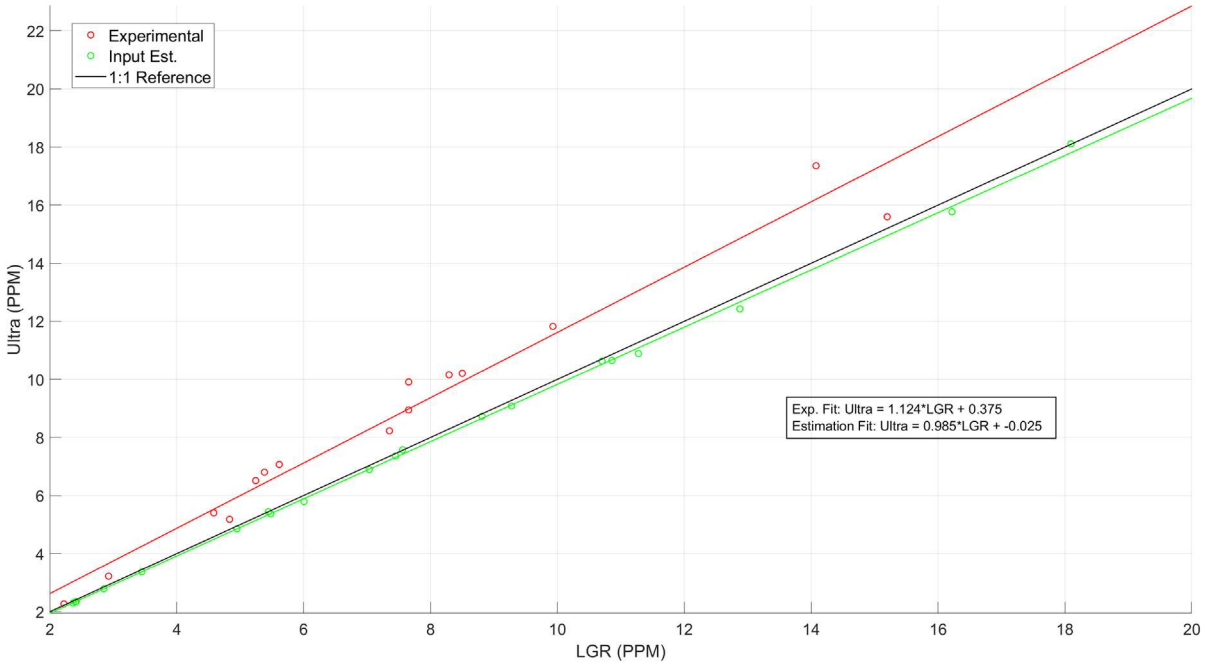

Figure 27. Scatter plot results from the stationary, 5 SLPM controlled release; the input estimation regime results in a slope of 0.985, very close to the measured steady-state slope.

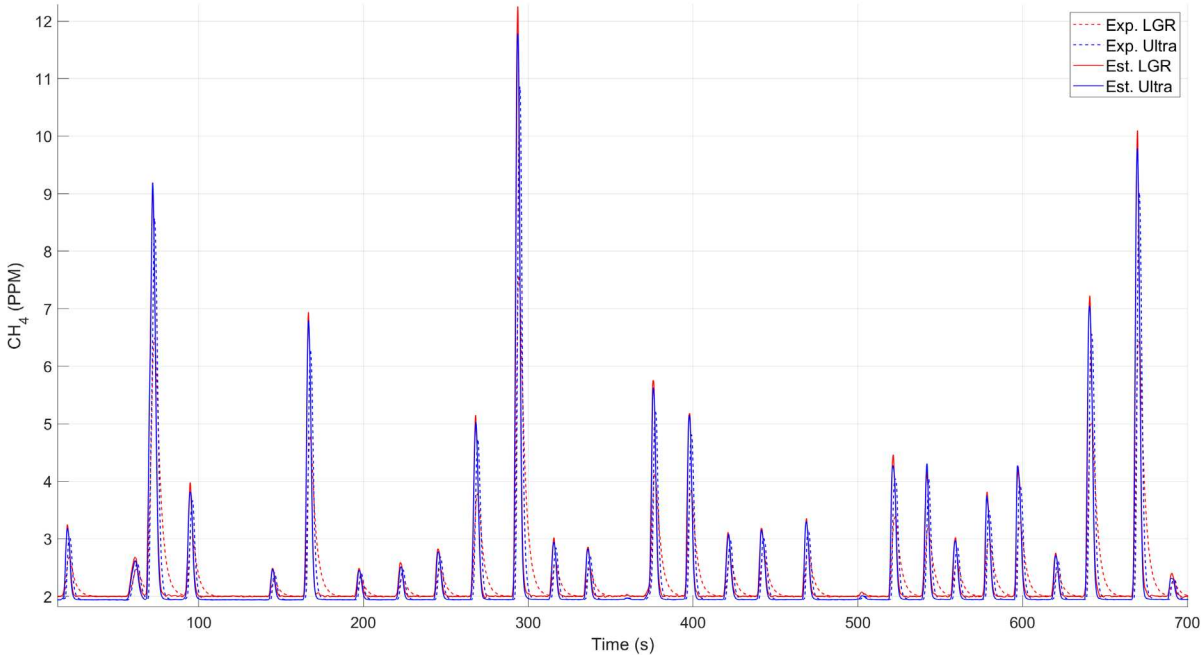

Figure 28. Instrument output and estimated signals from a 10 SLPM, moving-vehicle controlled release. Input estimate produces similar peak values and waveform shapes.

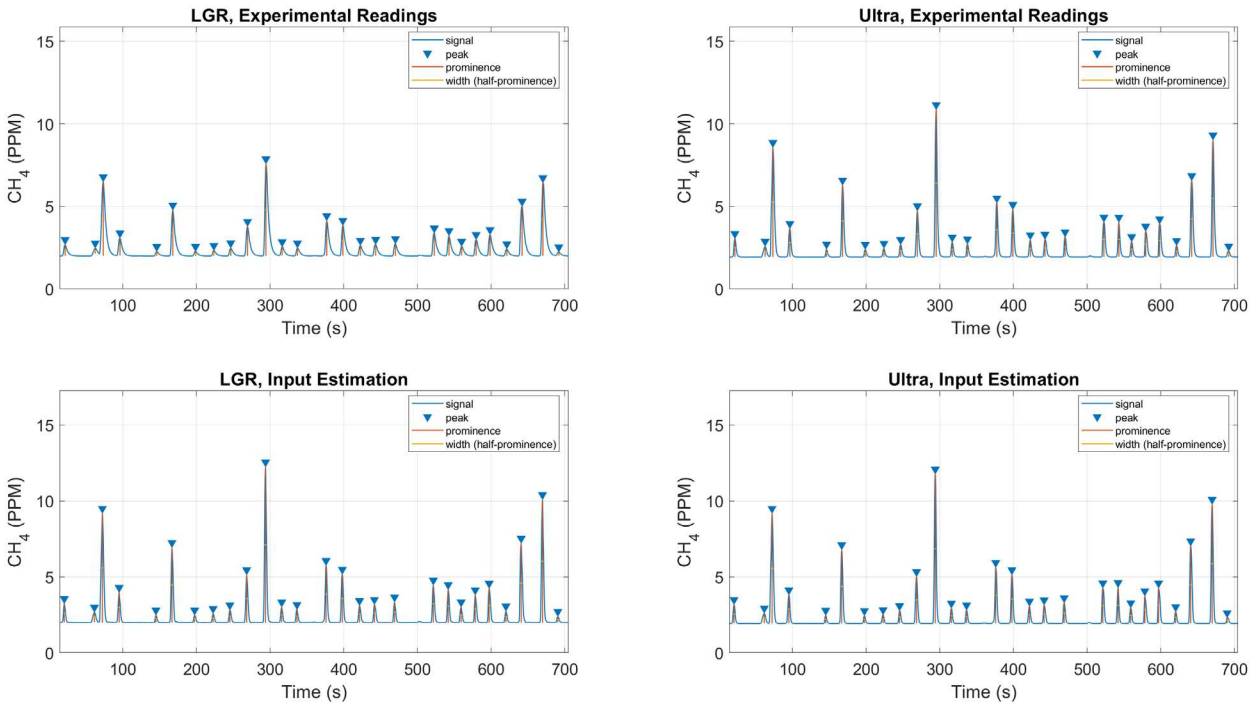

Figure 29. Peak analysis of the 10 SLPM, moving-vehicle controlled release. Note the improved similarity between the LGR and the Ultra signals after application of the input estimation procedure.

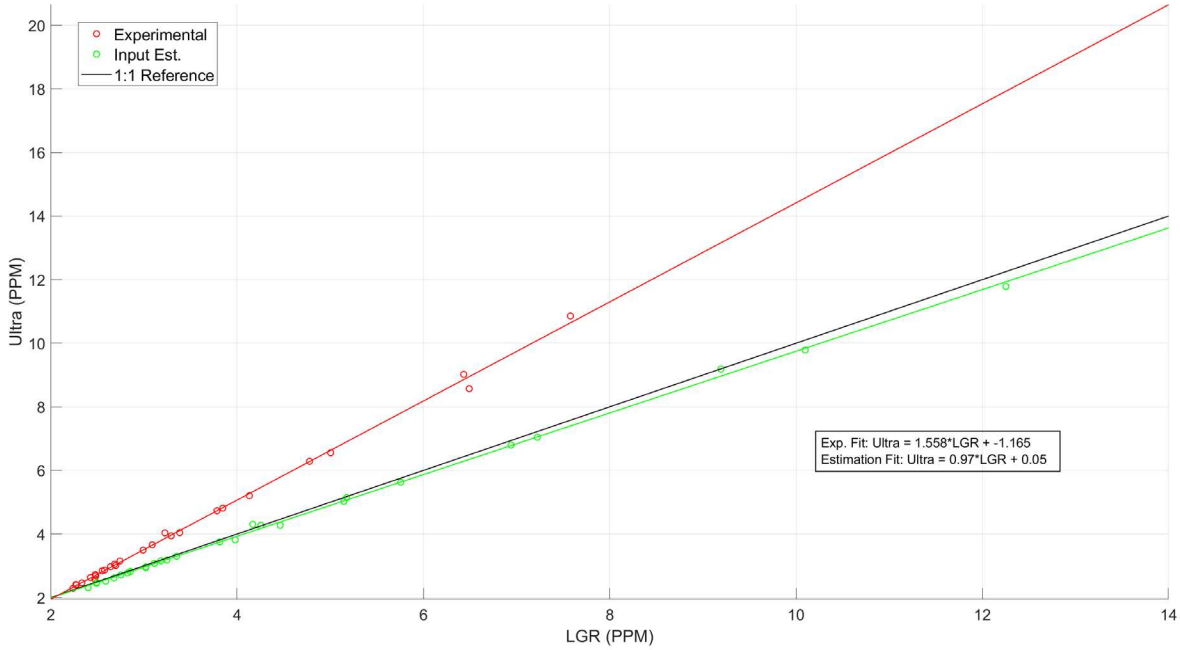

Figure 30. Scatter plot results from the 10 SLPM, moving-vehicle controlled release. The input estimation regime yields a slope of 0.97, again very close to the measured steady-state slope.

Numeric results from the various controlled release flow rates are summarized in Tables 3 and 4. For peaks greater than 2.2 PPM, a relation between the geometric mean of the *excess* CH4 peak values and the leak rate is posed by Weller [12], and the results of this relation using recently updated coefficients are listed in Table 3. For all but one case, the leak rate calculated using the estimation regime values result in an estimated leak rate closer to the true value. It should be noted that the coefficients included in the leak rate estimation were derived using raw instrument readings and did not consider the effects of the instrument time response. Therefore, the leak rate estimation should be considered as an example of the impact that only a few PPM difference of mean excess peak value can have on the estimated leak rate. For instance, the raw readings from the LGR during the 25 SLPM release report a leak rate of 8.76 SLPM and the corrected readings result in an estimated release rate of 15.38 SLPM, even though the geometric mean excess value only increased by 0.89 ppm. This sensitivity results from the fact that the estimated leak size is a logarithmic function of the mean peak values. This is a clear demonstration of the importance of accurately measuring true ambient gas concentrations, especially peak values, even when the difference between raw and estimated values occasionally appears to be small.

The number of matching peaks between the instruments increases for all flow rates, except the 10 SLPM test. As expected, the mean peak value increases for each instrument after the estimation is conducted, and the mean values of the respective instruments are closer to each other post-estimation. Both the ratio of the instruments, defined as the peak values of the Ultra divided by the matching peak values of the LGR, and the slope of the LGR vs Ultra plots decrease post-estimation. The post-estimation values indicate much higher agreement between the two instruments, though the slopes are still higher than the steady-state correlation values.

Table 4 also shows the mean peak difference, defined as the readings of the LGR minus the readings from the Ultra, based on corresponding instrument peaks, as well as the standard deviation of

Table 3 – Results from controlled release experiments

SLPM	# Matching Peaks	# Matching Peaks	LGR GeoMean (PPM)	Ultra GeoMean (PPM)	LGR GeoMean (PPM)	Ultra GeoMean (PPM)	LGR Estimated Leak Rate (SLPM)	Ultra Estimated Leak Rate (SLPM)	LGR Estimated Leak Rate (SLPM)	Ultra Estimated Leak Rate (SLPM)
	Exp.	Est.	Exp.	Exp.	Est.	Est.	Exp.	Exp.	Est.	Est.
50	21	22	2.80	4.22	5.37	5.23	18.50	30.37	40.75	39.48
25	22	24	1.52	2.34	2.41	2.39	8.76	14.86	15.38	15.20
10	27	27	0.99	1.51	1.71	1.68	5.19	8.70	10.13	9.93
5	22	23	0.59	0.89	0.86	0.85	2.78	4.56	4.41	4.34

Table 4 – Results from controlled release experiments (cont.)

SLPM	Mean Ultra/LGR	Mean Ultra/LGR	Slope	Slope	Peak Mean Diff. (PPM)	Std.dev of Diff (PPM)	Peak Mean Diff. (PPM)	Std.dev of Diff (PPM)
	Exp	Est.	Exp	Est.	Exp.	Exp.	Est.	Est.
50	1.279	0.973	1.550	0.961	-3.42	5.50	0.41	0.86
25	1.224	0.986	1.531	0.990	-1.02	0.74	0.07	0.13
10	1.178	0.981	1.558	0.970	-0.75	0.81	0.09	0.11
5	1.096	0.984	1.644	1.005	-0.27	0.26	0.05	0.02
Mean	1.194	0.981	1.571	0.981	-1.37	1.83	0.154	0.283

the difference. Again, it is shown that this mean difference, as well as the standard deviation decreases post-estimation.

Methodology Limitations and Considerations

It is important to highlight some of the limitations of the input estimation methodology. The first limitation is associated with the sampling rate of the instrument. In the analytical verification section, it was shown that with a very high sampling rate relative to the signal characteristics and a perfect output signal, the exact input signal can be reproduced, as shown in Figure 3. However, existing real-world instruments, especially instruments that characterize methane gas concentrations, have a sampling rate that is too low to perfectly reproduce the true input signal. As discussed, perfectly reproducing the input isn't the main goal because maximum gas concentrations in a peak have been found to be the most important factor in leak size estimation [12]. The ideal instrument has a fast sampling rate, fast response time, and high accuracy and precision. Unfortunately, this full combination

of instrument specifications is generally not available in methane gas sampling systems. For instance, while the Heath has a fast response time, it also has low accuracy and precision, especially for lower gas concentration values and it cannot report sub-PPM gas values.

The method for computing the correct zeta values is another consideration. As demonstrated, zeta can be computed by performing a test protocol like the one used in this research, shown for the LGR instrument in Figure 15. Zeta can be initially set to an arbitrarily high value and subsequently decreased until the average of the peaks generated by the input estimation is equal to the input values as defined in the test protocol. From here, the zeta values could be kept as a constant for all further analysis. Because the input estimation relies on accurate steady-state instrument readings, it is additionally necessary to ensure that instruments are calibrated properly. Due to the variety of instruments and their respective calibration approaches, using the input estimation regime to address instrument calibration is not considered, though it could be applied as a gain parameter within the transfer function.

Experimental setup must be considered as well. It is important to ensure that experimental instrument setup is as close to the instrument setup in the field data collection environment as possible. For instance, the tubing diameter used for the two setups should be the same, as the tube diameter has the potential to change the dynamics of the instruments or, at the very least, the amount of dead time between the inlet and the instrument response. Velocity of gas through the tubing increases with decreasing diameter, and the pressure drop increases with decreasing diameter. As a demonstration of the effects of diameter on the flow rate, the combined flow rate of the LGR and the Aeris Ultra was measured with both ¼" and 1/8" tubing. The combined flow rate was measured as approximately 1.24 SLPM with the ¼" tubing, and 1.14 SLPM with the 1/8" tubing. This slower flow rate could influence the results of the data and this discrepancy would need to be addressed if 1/8" tubing was required. All flow

measurements, characterization and field data collection in this research was conducted using the ¼" tubing.

CONCLUSIONS

Instrument response time is a phenomenon present in nearly all areas of instrumentation. Often the effects of response time are negligible or unimportant, especially where the measured quantity changes slowly over time compared to the instrument response time. However, when a slow response instrument is used to measure a quantity that can change quickly over time, the effects of instrument response time can become quite problematic. These effects have been demonstrated in this research, particularly in the LGR instrument, where peaks are dampened by the effects of its slow time response. Since the characterization of leaks is highly sensitive to the results of the sensor data, it is highly desirable to minimize the effects of the instrument time response. Furthermore, measurements made with instruments that have different time response characteristics result in discrepancies between their results. By performing carefully designed laboratory tests, the response characteristics of gas analyzers can be determined, allowing for an estimation of the true gas concentration input. An input estimation methodology was developed that yields corrected instrument response curves, compensating for the effects of the instrument time response, and resulting in a higher agreement between respective instruments.

Comparisons were made between the measurements recorded by Aeris Ultra and LGR instruments during controlled release experiments. The raw, experimental time-dependent readings recorded by the Aeris Ultra instrument were higher than the measurements made by the LGR instrument for every test condition. However, it was shown that the LGR instrument records higher steady-state values than the Aeris Ultra, but, because the Ultra has a faster time response, the Ultra reads higher peak values than the LGR during field measurements. As the leak rate increases, the difference between the two sensors readings increases, with the ratio of the sensors peak readings (Ultra/LGR) increasing from 1.096 at 5 SLPM to 1.279 at 50 SLPM. This discrepancy can also be

demonstrated as a mean difference between the readings of corresponding peaks (LGR – Ultra) in the data stream, which increase from -0.27 PPM at 5 SLPM to -3.42 PPM at 50 SLPM. When these corresponding peak readings are plotted as a scatter plot (LGR vs Ultra), an average slope of 1.571 is obtained over all of the test leak rates. Clearly, even though these instruments were sampling the same air, there is a significant difference in the raw readings of the instruments. These results form an excellent demonstration of the motivation for the goals of this research – to remove the discrepancy between gas analyzers.

After the estimation methodology is implemented, much of the difference between the sensors is removed. This is most clearly shown in the average slope of the comparison of the peak values detected by the LGR and the Ultra. The corrected data has a mean slope of 0.981, averaged over all the controlled released flow rates compared to 1.571 for the uncorrected data – a substantial improvement. Similarly, the effects of the estimation regime can be seen in the Ultra/LGR ratio, the peak mean difference, and standard deviation of the peak differences – all of which decrease, indication a much stronger agreement between the instruments. While the estimation slope is slightly higher than the steady-state slope (0.929), it is clear that the input estimation process eliminates much of the difference in readings between the instruments. As expected, the estimated peak readings are also higher than the raw experimental readings, indicating that, without the correction, the instruments underreport the true peak gas concentrations. This observation is an important since a difference of only a few PPM in the peak value can strongly affect the estimation of leak size.

This research has provided a clear demonstration of the effects that response time can have on instrument readings and the disagreements that can result between different instruments. Results have demonstrated that by characterizing the instruments using auxiliary laboratory tests and using the estimation methodology developed in this work, measurement accuracy can be significantly improved and much of the instrument-to-instrument disagreements can be removed. In addition, estimation of

methane leak size based on field measurements can be refined. This estimation procedure will be applied to further methane mapping efforts, where its effects on the estimation of leak size and location can be further quantified.

REFERENCES

1. Balcombe, P., et al., *The Natural Gas Supply Chain: The Importance of Methane and Carbon Dioxide Emissions.* ACS Sustainable Chemistry & Engineering, 2017. **5**(1): p. 3-20.
2. Lelieveld, J., P.J. Crutzen, and C. Brühl, *Climate effects of atmospheric methane.* Chemosphere, 1993. **26**(1): p. 739-768.
3. Pachauri, R.K., et al., *Climate Change 2014: Synthesis Report. Contribution of Working Groups I, II and III to the Fifth Assessment Report of the Intergovernmental Panel on Climate Change*, ed. R.K. Pachauri and L. Meyer. 2014, Geneva, Switzerland: IPCC. 151.
4. Jeong, S., et al., *Estimating methane emissions from biological and fossil-fuel sources in the San Francisco Bay Area.* Geophysical Research Letters, 2017. **44**(1): p. 486-495.
5. Zazzeri, G., E. Yeomans, and H. Graven, *Global and Regional Emissions of Radiocarbon from Nuclear Power Plants from 1972 to 2016.* Radiocarbon, 2018. **60**.
6. Hmiel, B., et al., *Preindustrial 14CH4 indicates greater anthropogenic fossil CH4 emissions.* Nature, 2020. **578**(7795): p. 409-412.
7. Alvarez, R.A., et al., *Assessment of methane emissions from the U.S. oil and gas supply chain.* Science, 2018. **361**(6398): p. 186-188.
8. Phillips, N.G., et al., *Mapping urban pipeline leaks: Methane leaks across Boston.* Environmental Pollution, 2013. **173**: p. 1-4.
9. Jackson, R.B., et al., *Natural Gas Pipeline Leaks Across Washington, DC.* Environmental Science & Technology, 2014. **48**(3): p. 2051-2058.
10. Weller, Z., et al., *Vehicle-Based Methane Surveys for Finding Natural Gas Leaks and Estimating Their Size: Validation and Uncertainty.* Environmental Science & Technology, 2018. **52**.
11. von Fischer, J.C., et al., *Rapid, Vehicle-Based Identification of Location and Magnitude of Urban Natural Gas Pipeline Leaks.* Environmental Science & Technology, 2017. **51**(7): p. 4091-4099.
12. Weller, Z.D., D.K. Yang, and J.C. von Fischer, *An open source algorithm to detect natural gas leaks from mobile methane survey data.* PloS one, 2019. **14**(2): p. e0212287-e0212287.
13. McCarthy, J., *A Method for Correcting Airborne Temperature Data for Sensor Response Time.* Journal of Applied Meteorology and Climatology, 1973. **12**(1): p. 211-214.
14. Arieli, R. and H.D. Van Liew, *Corrections for the response time and delay of mass spectrometers.* J Appl Physiol Respir Environ Exerc Physiol, 1981. **51**(6): p. 1417-22.
15. Wong, L., et al., *A real-time algorithm to improve the response time of a clinical multigas analyser.* J Clin Monit Comput, 1998. **14**(6): p. 441-6.
16. Takriti, M., et al., *Mobile methane measurements: Effects of instrument specifications on data interpretation, reproducibility, and isotopic precision.* Atmospheric Environment, 2020: p. 118067.
17. Sirs, J.A., *A method of correcting for the response time delays of measuring equipment.* Journal of Scientific Instruments, 1958. **35**(11): p. 419-422.

APPENDIX A. 3D PLUME ANALYSIS

During controlled release field testing, an anemometer array, Figure A1 consisting of five 3D, sonic anemometers was utilized to catalogue the wind conditions (magnitude and direction) during testing. These five anemometers are configured in a linear vertical array at heights of 1, 2.5, 5, 8.5, and 11 feet above the ground, which provides insight to the velocity gradient as a function of height. Near the ground, boundary layer effects are dominant, creating a layer of slower wind speeds. As the height increases, so does the wind velocity. These effects play a significant role in the plume dynamics of a leak. Additionally, the fourth anemometer of the array is located at the same height as the anemometer on the vehicle, allowing a direct comparison to be made between the windspeed calculated from the vehicle and the windspeed from the array, which will be discussed later. To better understand the effects of wind and boundary layers on the behavior of the plume, a 3D computational fluid dynamics (CFD) model was created. This model takes in the data from the five sensors and interpolates between

Figure A1. An anemometer array consisting of five, 3D sonic anemometers.

them, using the wind profile power law, to create a smooth gradient of wind speeds as a function of height. Once the height of the domain is above the height of the last sensor on the array, the wind value remains constant. This profile is used as the flow inlet boundary condition in the CFD model.

The CFD model consists of a 3D domain, with one corner of the domain representing the location of the anemometer. From here, the two faces perpendicular to this location are considered to be the inlets of the model, with the opposite two faces considered to be the outlets. Figure A2 shows the velocity profile at one of the inlet faces of the model and demonstrates the use of the wind profile power law as an interpolation method. A representative velocity profile for one instant in time is shown in Figure A3. The lower face, or 'ground', of the model is set to be a no-slip boundary condition, meaning the wind velocity immediately at the ground surface is zero, and the upper face, or sky, is set to be a zero-shear condition. The domain of the model is rotated about the z-axis so that the prevailing winds of the data flow towards the outlet. This helps ensure the flow is continuous throughout the model. The domain is meshed using polyhedrons, with elements nearing the inlets decreasing in size. The mesh created for one of these models can be seen in Figure A4. Additionally, a point source of

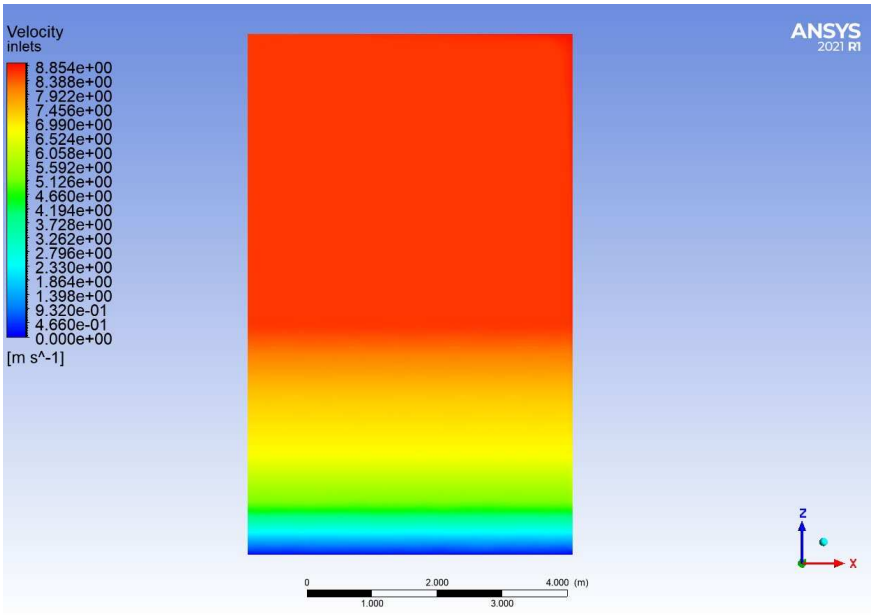

Figure A2. Velocity profile at an inlet face for a 3D plume simulation, demonstrating the wind profile power law.

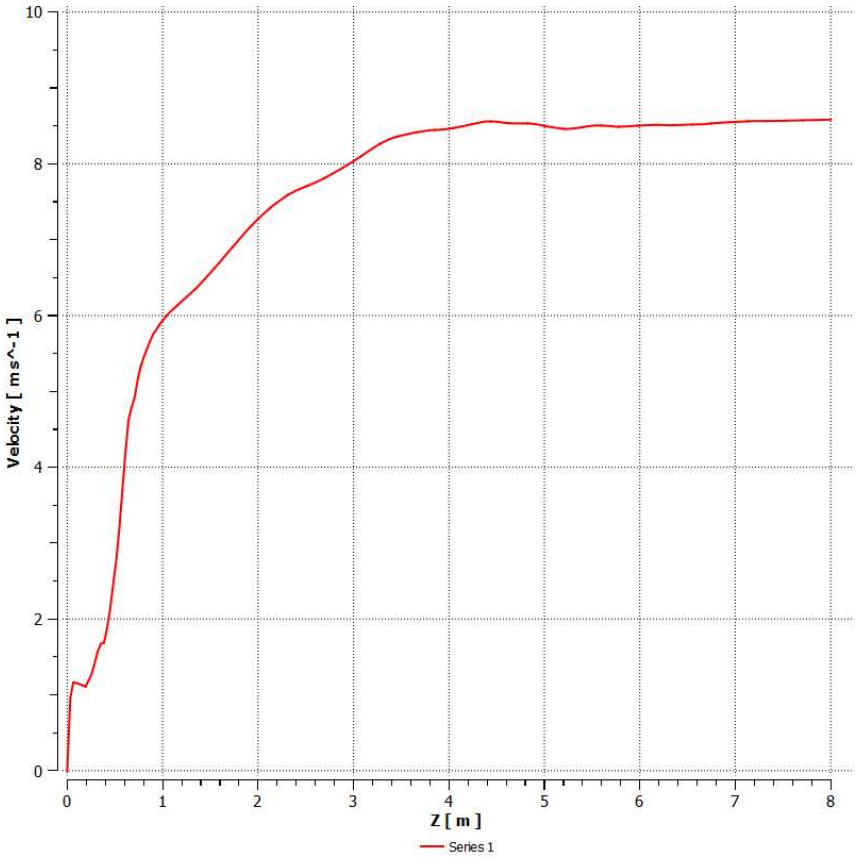

Figure A3. Representative wind velocity profile as a function of height at an inlet.

methane is located on the ground face (z = 0) of the model in the approximate location relative to the anemometer in the real-world test. The methane leak rate in the model is set to be whatever the actual leak rate was set to during the real-world test. The goal of this model was to provide a realistic simulation of the plume dynamics using real-world dynamic wind data.

The simulation is calculated using a k-epsilon turbulence model, with turbulent and gravitational forces considered. Since the wind data from the array is sampled at 10Hz, the model is simulated at this rate as well. That means that for every time step of 0.1s, the model will take the respective real-world wind readings from that time, interpolate the sensors with the wind profile power law, and apply this measurement to the inlet conditions. A save state of the model is created every 5 seconds, allowing animations of the plume to be created over time. An example of the plume simulation at one point in

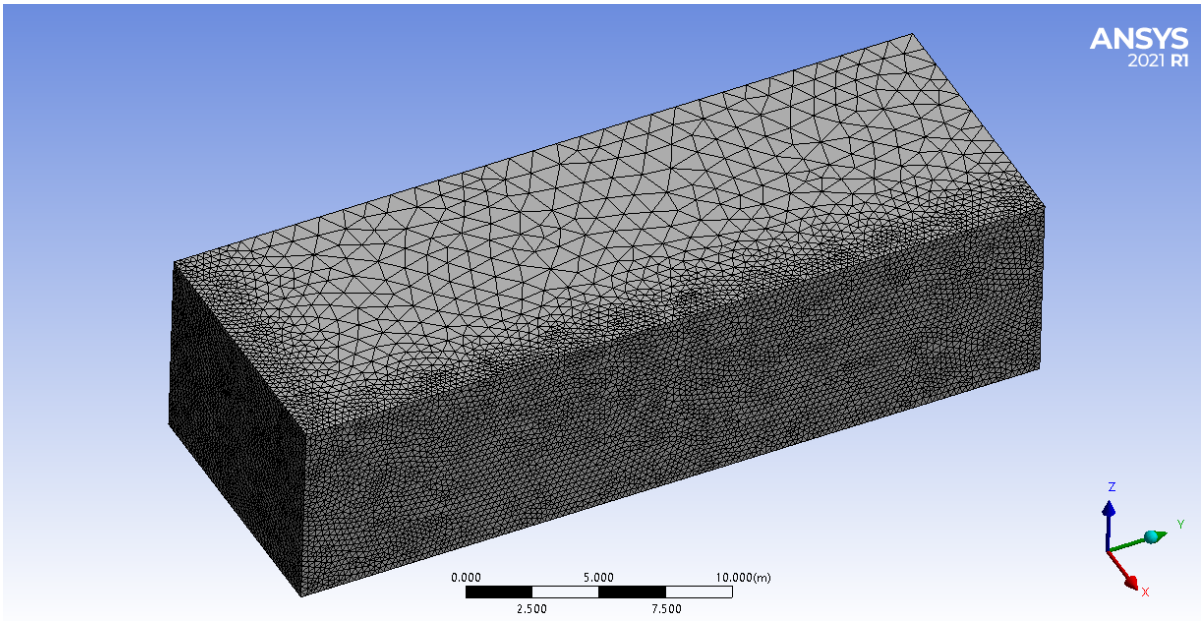

Figure A4. Polyhedral mesh for 3D CFD plume simulation.

time is presented in Figure A5. The dynamic wind effects on the plume can clearly be seen, especially with regard to the decreasing local concentrations and the dispersion of the gas in the flow direction.

While the simulation shows the general dynamics of the plume in real-world conditions, both the simulation environment and the test site of the controlled release, are idealized conditions. The real-world data were collected at environments similar to the model conditions – at an airstrip devoid of any obstacles or trees, though some thicker brush does exist off the sides of the airstrip. In the real-world, a variety of factors affect the plume dynamics, such as the surface conditions. For instance, the leak could be rising from a relatively smooth surface, such as pavement, or from a complex layer, such as thick brush. Leaks can even come from under the ground, rather than right at the surface level, creating a kind of porous dispersion effect. In cities, buildings, trees, and other obstacles have a large impact on the dynamics of the plume. These models, depending on the size of the domain, take a considerable amount of computational time, even in the relatively simple, idealized setting. Adding obstacles or other more advanced features would add significant amounts of computational time. Additionally, many more meshing and algorithm strategies must be considered for complex models to produce accurate results.

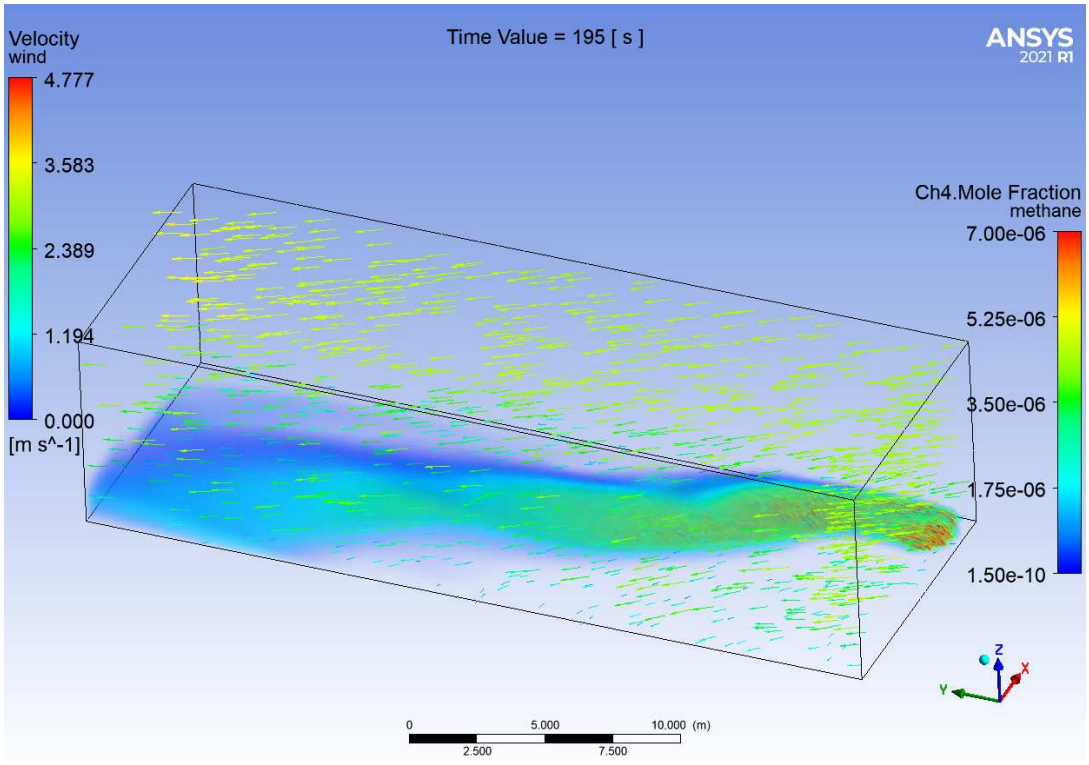

Figure A5. 3D CFD plume simulation results showing methane mole fractions and wind vectors.

Nevertheless, CFD modelling does prove to be a useful resource, and could be used, if the proper considerations are made, to simulate the behavior of leaks in more complex and realistic environments. For instance, points, or a collection of points, called rakes, can be inserted into the domain of the model. This way, various parameters, such as wind speed or CH4 PPM values, can be measured at these locations over time. During controlled release tests, the car will pass by the leak at a variety of prescribed distances, making the same pass multiple times. By inserting rakes at these same locations within the model, the CH4 values estimated within the model can be compared to the real-world measurements, made at the same point in time. An example of data acquired from these virtual rakes is shown in Figure A6, using a background CH4 value of 0 PPM. However, syncing readings between the vehicle with computed values from the model along space and time is a very difficult task. The most accurate method would involve a probe point within the model, that constantly tracks the

vehicle's position in time. This probe measurement would allow comparisons to be made at the correct geospatial location. Still, additional complications would be present with this method. The vehicle's gas concentration measurements are time-delayed, and the on-board instrument only records at 1Hz. Together, all these complications make direct comparisons between the CFD model and the car's readings extremely difficult. The CFD results are useful, however, in enabling visualization of the complex nature of natural gas plume dispersion.

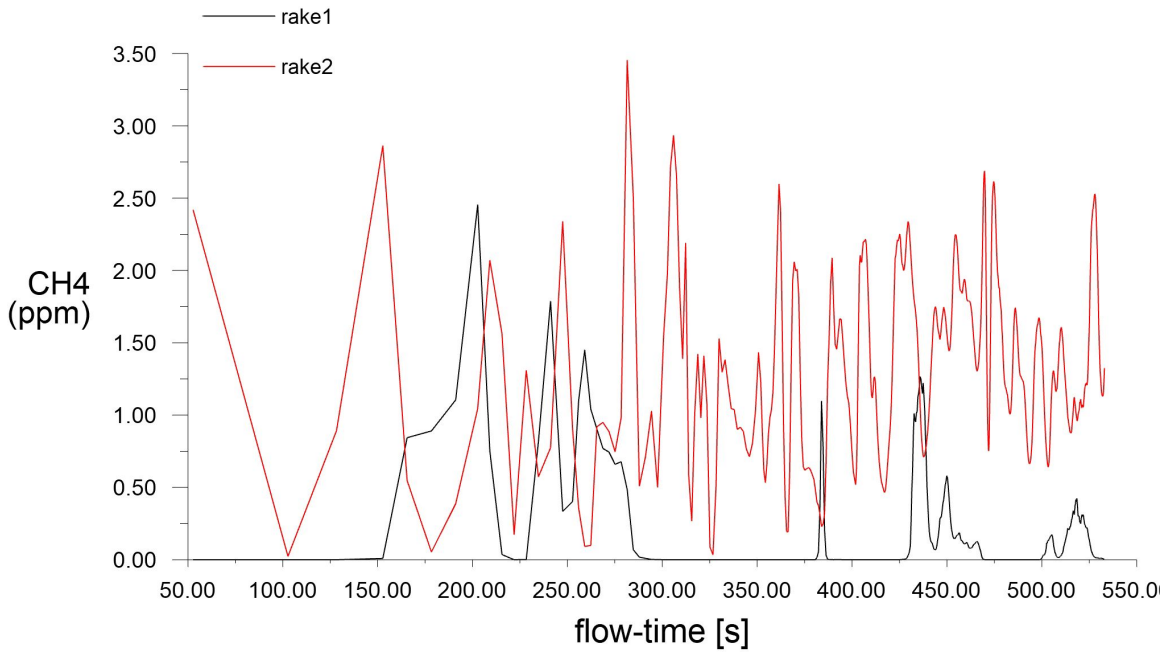

Figure A6. Average of CH4 concentration values along two stationary rakes over time, from CFD simulation.

APPENDIX B. WIND CORRECTIONS FROM VEHICLE

As previously discussed, an anemometer is located on the vehicle, recording relative wind data during controlled release and survey data collection. The purpose of the anemometer is to record the meteorological conditions to better understand its effects on plume dynamics, as well as to aid in locating the source of the leak. However, since this anemometer is on a moving vehicle, accurately deciphering the true wind conditions based on the vehicle anemometer readings at a given location is difficult. Theoretically, the readings from the anemometer are a combination of the true wind conditions, combined with addition of the apparent wind generated by the moving vehicle and, by subtracting the vehicle's motion from the anemometer readings, the true wind conditions can be found. However, this is not the case, and simply removing the car's motion does not produce wind readings that match well with the readings obtained from the stationary anemometer. This discrepancy is associated with flow distortion effects around the vehicle itself. During vehicle motion, air passes over the vehicle and, due to the aerodynamic effects, accelerates to values larger than the vehicle's actual speed. To better understand these effects, a 2D CFD model was generated using the test vehicle's geometry. The model consists of a 2D model of the car inside a rectangular domain, which, in essence, simulates a 2D vehicle representation in a wind tunnel. Results of the flow simulation are presented in Figure B1, where the vehicle's speed is set to 8.5m/s. The local flow field and wake effects of the vehicle's geometry can clearly be seen. The vehicle's anemometer is approximately located above the top of the windshield. A velocity probe point was placed in the model at the approximate location of the vehicle-mounted anemometer. The measured velocity from the simulation at this location is ~12.6m/s, much higher than the vehicle's true velocity. Consequently, if only the vehicle's velocity is removed from this measurement, the anemometer reading would be an overestimation. By varying the car's velocity in

this simulation, a linear relationship can be determined for the apparent velocity at the anemometer as a function of car velocity, as seen in Figure B2. However, there are limitations of this model. Since the

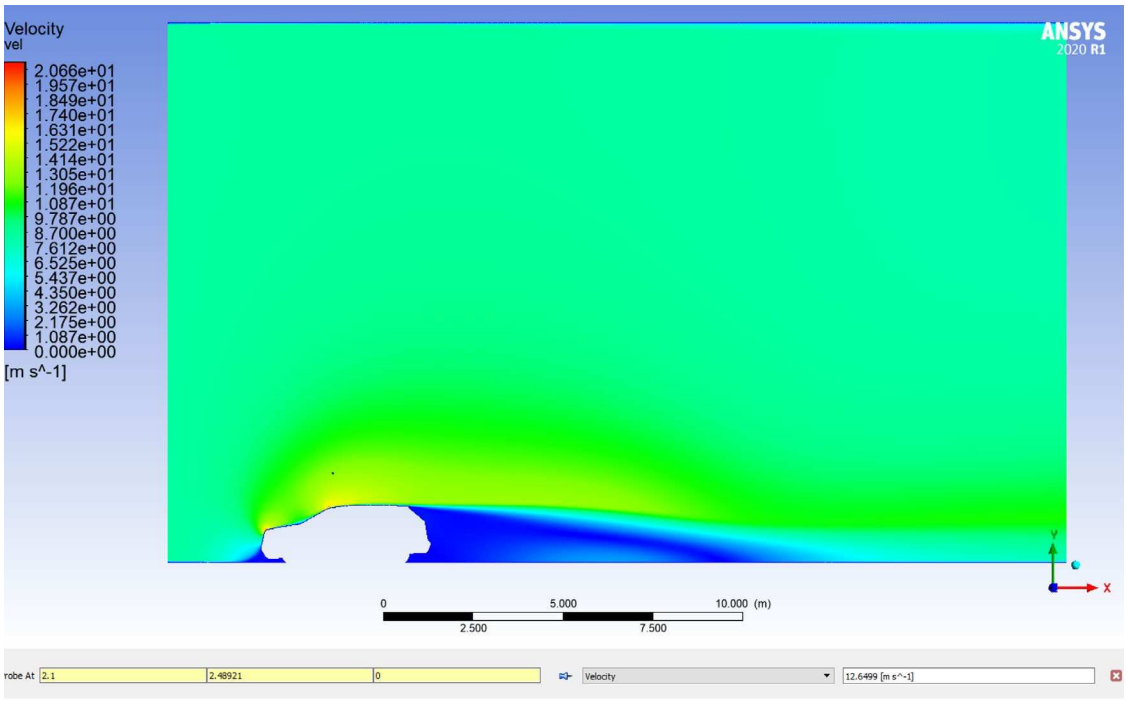

Figure B1. Velocity field from 2D CFD simulation of the methane mapping vehicle driving at 8.5m/s.

model is only in 2D, it can only simulate the aerodynamic effects from the front to the back of the vehicle. In essence, the model is a simulation of the vehicle driving with zero ambient wind. In the real world, wind can be flowing over the car from any direction. The 3D aerodynamic effects of wind flowing over the side of the car will be different than the effects of wind flowing from the front to the back. Therefore, while the model demonstrates the effects of localized flow around the vehicle, it does not necessarily predict the complex air dynamics that occur over the vehicle in real world testing.

To determine how best to correct the car's flow field effects, field data collected from the airstrip was analyzed. At the airstrip, the vehicle is driven back and forth along the runway. The stationary anemometer array is set up at the midpoint along the length of the runway. This location allows wind data to be collected both as the car gets closer and further away from the array. As

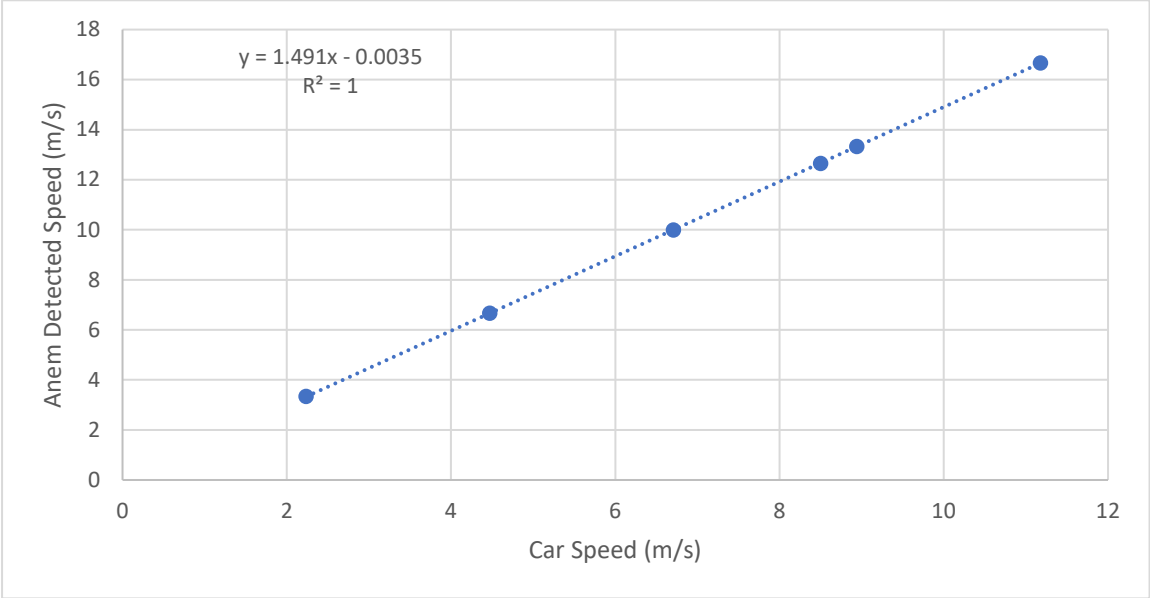

Figure B2. Linear relationship between the simulated car velocity and the velocity reading at the anemometer's location.

mentioned previously, the airstrip is located in a flat area, and is mostly obstruction-free, allowing the assumption that the wind at the car's location and the wind at the array will be relatively similar. Wind magnitude and direction data collected from one of these tests are presented in Figure B3 and Figure B4, respectively. These figures show the corrected wind magnitude and direction calculated at the car with only the vehicle's motion front-to-back component subtracted – no bias or local flow field effects are taken into consideration. While the corrected wind magnitude at the car is sometimes similar to the wind magnitude detected at the array, the difference between the two increases and decreases in a sort of oscillating pattern, even though the vehicle speed is subtracted from the data. This is most likely due to the fact that the car is sometimes heading into the wind and sometimes heading with the wind. The vehicle flow distortion effects vary depending on whether the vehicle is experiencing a headwind or a tailwind.

To further compare the wind collection data, the car's velocity is again subtracted from the apparent wind data collected from the moving vehicle's anemometer. Then, the wind measurements at

the fourth sensor on the stationary array (the sensor that is at the same height as the car's anemometer) are numerically rotated, such that N/S component of wind is in line with the front-to-back

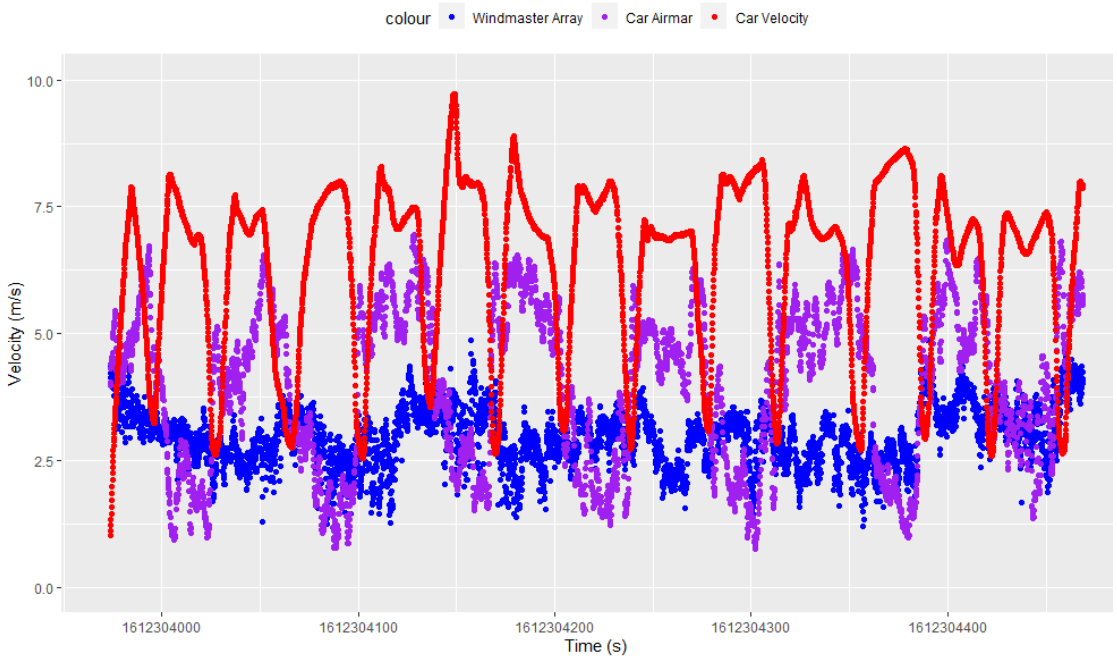

Figure B3. A five-minute slice of data collected at METEC, showing the car's velocity, the car's wind speed reading after vehicle's speed is removed, and the wind speed at the fourth sensor on the anemometer array.

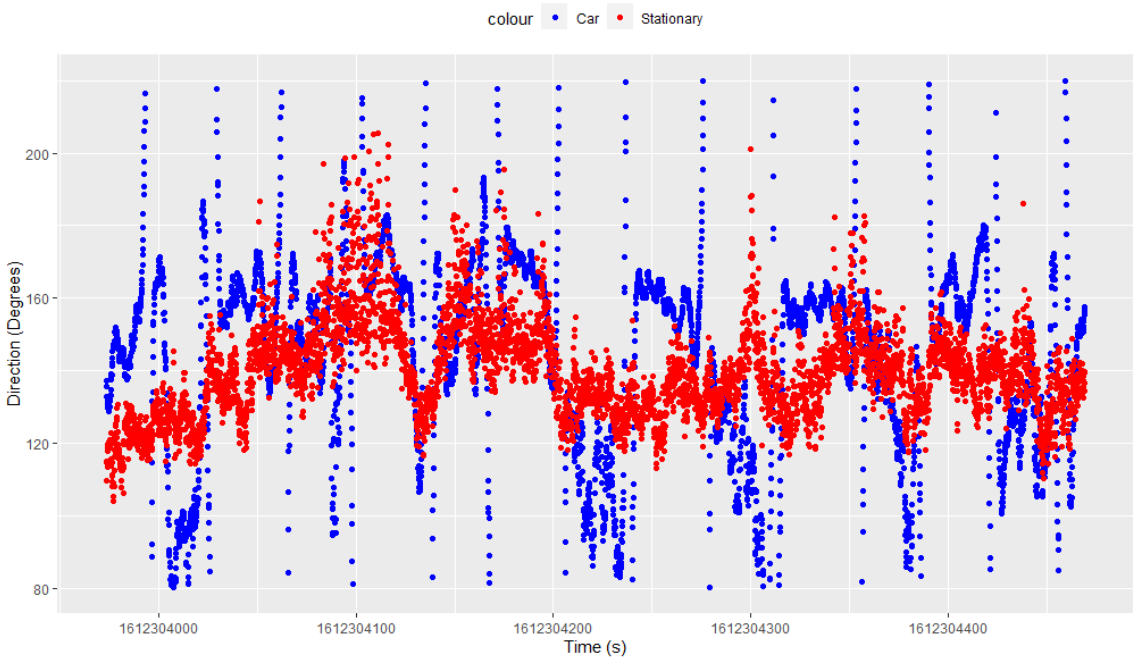

Figure B4. A five-minute slice of data collected at METEC, showing the wind direction calculated at the car and at the fourth sensor on the anemometer array.

direction of the car, and the E/W component is in line with the side-to-side direction of the car. This rotation allows the difference between the two sensors to be directly calculated along these components. This difference is plotted, along with linear fits, in Figure B5 and Figure B6 as a function of the corrected vehicle-measured speed. Negative values of the x coordinate in these figures generally correspond to the vehicle traveling against the wind, while positive values generally indicate vehicle travel with the ambient wind. However, recognizing the flow field distortion in the vehicle-mounted anemometer readings discussed previously, some data points with positive corrected wind speed values on the x-axis may correspond to cases where the vehicle is actually traveling against the ambient wind. For perfect agreement, the difference between the corrected vehicle reading and the reading from the stationary anemometer (y-axis) would be zero for all vehicle speeds. However, Figure B5 indicates a

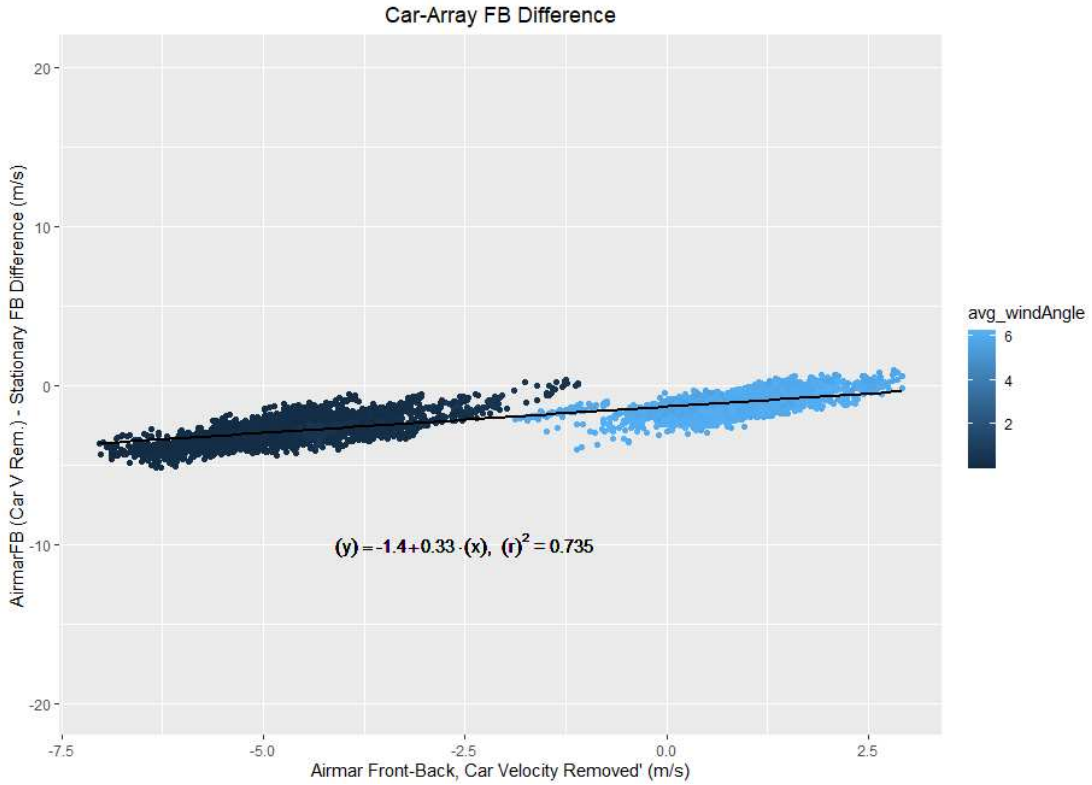

Figure B5. Plot of the difference in vehicle front-to-back wind speed and the corresponding wind speed from the stationary array, as a function of the corrected front-to-back vehicle wind speed.

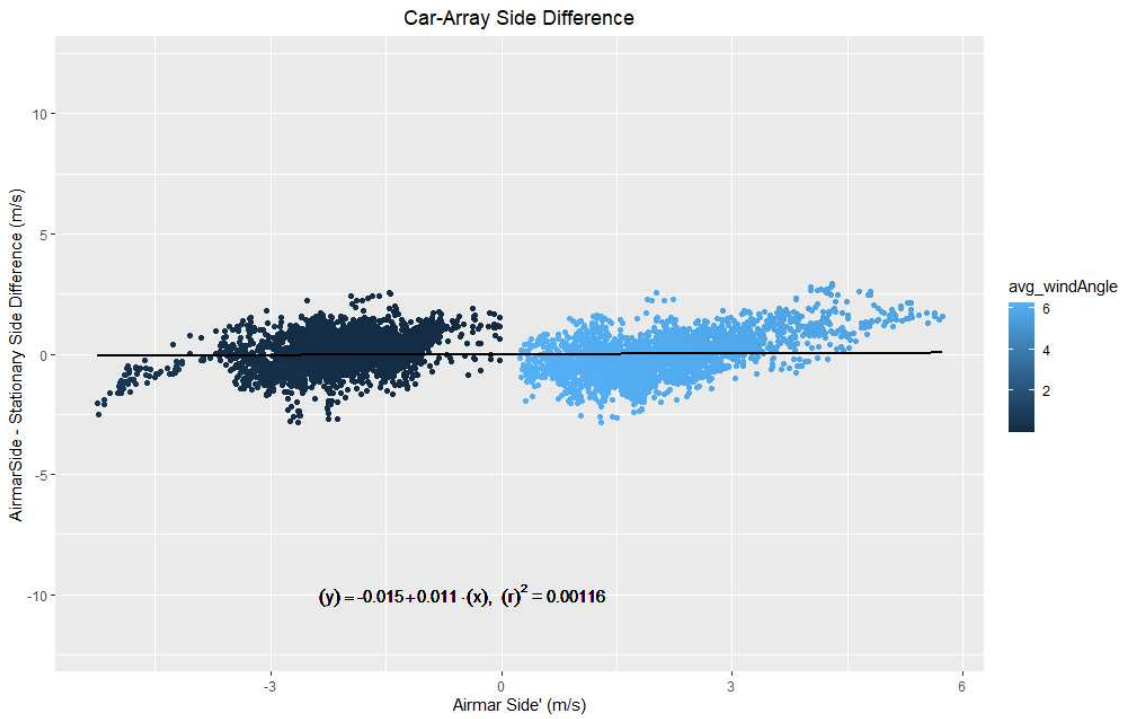

Figure B6. Plot of the difference in wind speed detected from the side of the car, detected at the car and stationary array, as a function of the side wind speed detected at the car.

strong nonzero positive slope trend in the difference between the two sensors along the vehicle front-to-back component, but not a lot of difference (no strong correlation) with the side component.

The data points plotted in these two figures are also colored by the average, uncorrected detected wind angle, in radians, on the vehicle. While in motion, this angle is almost always near zero degrees, as this is the car's 'northern' direction, and wind will flow from the front-to-back of the vehicle during travel, with the apparent wind velocity associated with the vehicle speed generally higher than the true wind speed measured at the stationary array. However, depending on the car's direction of travel, and the direction of the true wind, this value can switch from being more to the right side of the vehicle (slightly greater than zero degrees or zero radians), or to the left (slightly less than 360 degrees, or 2π radians). There is a clear relationship between the uncorrected wind angle and the car's direction of travel relative to the true wind. For this data set, when the vehicle is traveling with the wind (generally positive x-axis value), the detected flow angle is slightly less than 2π radians (blue color code),

meaning that the crosswind has an easterly component with respect to the vehicle reference frame. When the vehicle is traveling against the wind, the crosswind therefore must have a westerly component, as indicated in the figure with flow angles coded at slightly above 0 radians (Black).

The least-squares linear data fit equation shown in Figure B5 can be used as a bias correction for the data set. Since the equation provides the difference between the corrected wind speed detected on the vehicle (with the vehicle's velocity removed) and the stationary anemometer, it can be applied as an offset correction. The results of applying this offset correction are presented in Figure B7 and Figure B8. These results show a much better agreement between the vehicle-mounted anemometer and the stationary array. There are still a few small regions of error, which relate to the regions where the vehicle is turning. Since the vehicle's velocity and bearing are calculated by using an onboard GPS, errors can be generated when the vehicle's velocity is too slow, or when the vehicle is turning.

Unfortunately, the offset correction values seem to change from data set to data set. This phenomenon has been observed in many different data sets, and is most likely due to different wind

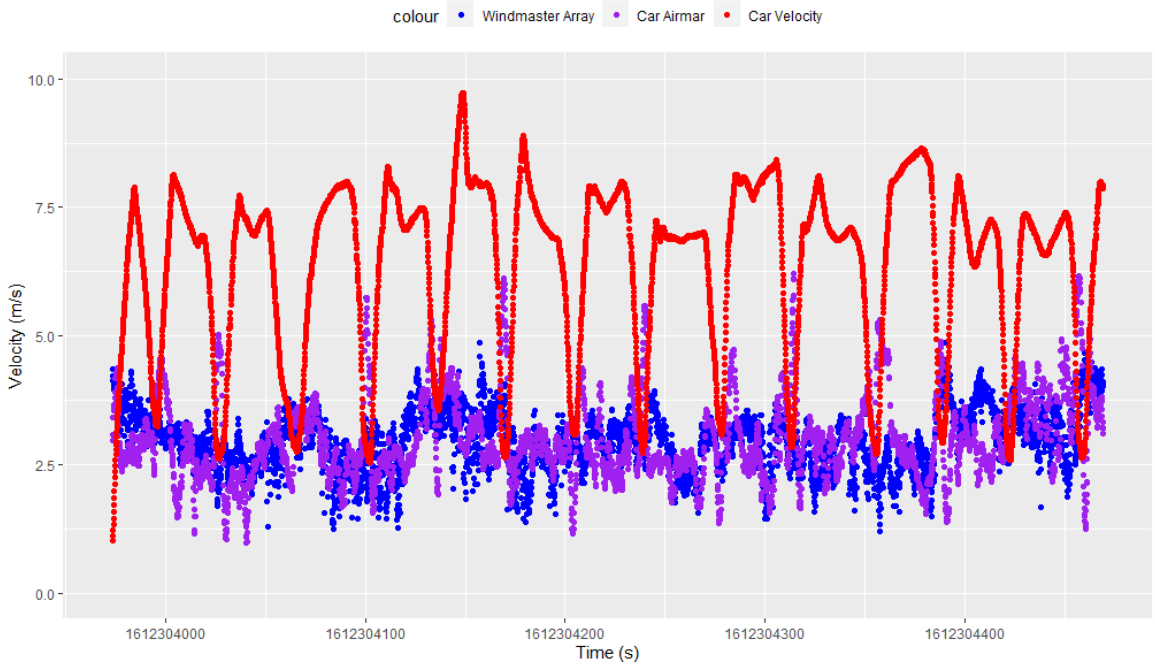

Figure B7. A five-minute slice of data collected at METEC, showing the car's velocity, the car's wind speed reading after vehicle's speed is removed and correction offset applied, and the wind speed at the fourth sensor on the anemometer array.

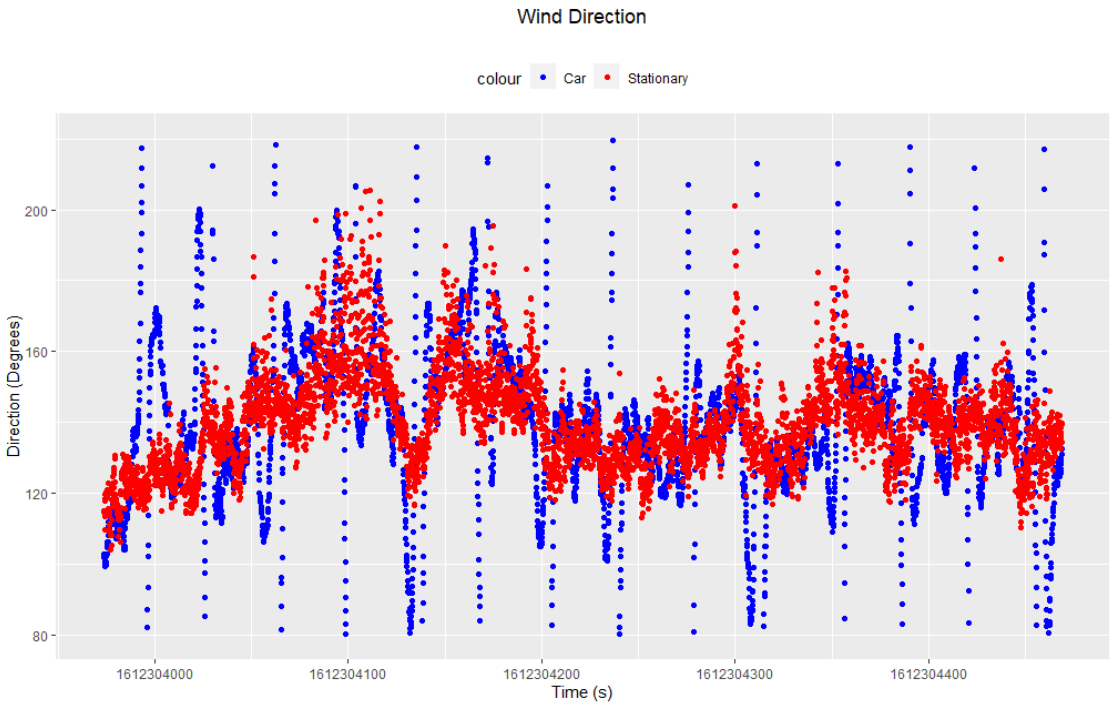

Figure B8. A five-minute slice of data collected at METEC showing the wind direction calculated at the car after correction offset is applied and at the fourth sensor on the anemometer array.

conditions, as well as driving locations. METEC is a very flat area with few obstructions to cause variances in the wind over small distances. At other locations where this analysis was performed, such as in a neighborhood, the wind is much more variable over the same distance. It is expected that even more complex environments, such as busy roads in larger cities, will produce even more variable wind data. While it is not necessary for the car's anemometer to perfectly reproduce the values taken on the stationary array, and true wind values will be unknown during actual survey efforts, it is desirable that at least the general wind direction indicated by the two instruments are similar. While wind speed is an important component for plume dispersion, wind direction can give a better idea of where the leak may be coming from. Research is currently being conducted to find a pattern for the best correction values to accommodate these discrepancies.